Thermal Science and Engineering Progress 42 (2023) 101772

Contents lists available at ScienceDirect

Thermal Science and Engineering Progress

journal homepage: www.elsevier.com/locate/tsep

Thermal radiation at high-temperature and high-pressure conditions: Comparison of models for design and scale-up of entrained flow gasification processes

Maximilian Dammann [a,b,c,1], Marco Mancini [c], Thomas Kolb [a,b], Roman Weber [c]

[a] Karlsruhe Institute of Technology (KIT), Engler-Bunte-Institute, Fuel Technology (EBI ceb), Engler-Bunte-Ring 1, 76131 Karlsruhe, Germany
[b] Karlsruhe Institute of Technology (KIT), Institute for Technical Chemistry, Gasification Technology (ITC vgt), Herrmann-von-Helmholtz-Platz 1, 76344 Eggenstein-Leopoldshafen, Germany
[c] Clausthal University of Technology, Institute for Energy Process Engineering and Fuel Technology (IEVB), Agricolastrasse 4, 38678 Clausthal-Zellerfeld, Germany

ARTICLE INFO

Keywords:
Radiative heat transfer
High pressure
CFD
Entrained flow
Gasification

ABSTRACT

Thermal radiation is an important sub-process in high-pressure entrained flow gasification. However, it was seldom investigated in previous CFD studies and was usually accounted for by common radiation and simplified gas radiation property models. Therefore, this study performed comparative one-dimensional radiation and two-dimensional CFD simulations with respect to the bioliq Entrained Flow Gasifier (bioliq EFG). The one-dimensional radiation simulations were applied to compare the effects of advanced and simplified gas radiation property models for atmospheric and high-pressure entrained flow gasification conditions, while the CFD simulations were carried out to investigate the performance of simplified gas radiation property models incorporated within the CFD model of the bioliq EFG. The segmental heat removal from the cooling screen of the bioliq EFG was applied as experimental basis for comparison with the numerical predictions. Based on the comparisons, this study provides recommendations for the selection of gas radiation property models for CFD simulations with the discrete ordinates model and with focus on entrained flow gasification. In case of largely isothermal and homogeneous conditions with exemption of the flame zone, weighted-sum-of-grey-gas models can be used with the discrete ordinates model if user-defined weighted-sum-of-grey-gas models (i) are obtained from accurate line-by-line calculations, (ii) are based on conditions prevailing in the reactor and (iii) are incorporated using the band approach. In absence of such weighted-sum-of-grey-gas models, full-spectrum correlated-k distribution models based on the latest tabulations can be used instead for CFD simulations of entrained flow gasification processes. In addition to that, sensitivity analyses showed that a coarse discretisation of the radiative transfer equation within the boundary layer, inaccurate gas species concentrations in the boundary layer (within a $\pm 5\%$ margin) and the P-1 approximation can be accepted for high-pressure conditions while soot radiation becomes important at soot volume fractions above 10^{-6} and should be accounted for if such conditions are expected.

1. Introduction

Entrained flow gasification processes are applied to convert carbonaceous fuels to synthesis gas at high-temperature conditions. In order to replace the current fossil fuel-based technologies in the foreseeable future, new biomass-based technologies, as the bioliq process [1], and new flowsheet and CFD models are under development [2–7]. Gas atmospheres in these processes are characterised by large contents of water vapour, carbon dioxide and carbon monoxide. Thermal radiation is thus the dominant mode of heat transfer and needs appropriate mathematical description. However, previous CFD studies on entrained flow gasification relied on simplified or readily available grey-gas absorption coefficient models. Lu et al. [8] applied unspecified piecewise polynomials while Marklund [9] assumed constant values of 15 m^{-1} and 30 m^{-1} based on simple high-pressure scaling of an atmospheric gas absorption coefficient to investigate the effects on the gas temperature. Furthermore, the gas absorption coefficient was frequently [10–28]

[1] Corresponding author. ORCID: http://orcid.org/0000-0002-2851-7787.

https://doi.org/10.1016/j.tsep.2023.101772
Received 30 September 2022; Received in revised form 27 January 2023; Accepted 27 February 2023
Available online 5 March 2023

Nomenclature

Latin symbols

a	weight in the pseudo-band models
$\boldsymbol{a}$	weight vector in the pseudo-band models
A	area
C	absorption cross-section
$\boldsymbol{C}$	absorption cross-section vector
C	constant
$\dot{e}$	emissive power
f	fraction
F	absorption line blackbody distribution function
G	incident radiation
I	intensity
K	absorption coefficient
$\boldsymbol{K}$	absorption coefficient vector
L	length
n	number of half-widths
$\boldsymbol{n}$	normal vector
p	pressure
$\dot{q}$	heat flux
S	source term
T	temperature
V	volume
w	quadrature weight
$\boldsymbol{w}$	quadrature weight vector
X	auxiliary variable
x	mole fraction
$\boldsymbol{x}$	mole fraction vector
z	position
$\boldsymbol{z}$	position vector

Greek symbols

α	transformation factor
Δ	difference
ε	emissivity
η	wavenumber
μ	discrete ordinate
$\boldsymbol{\mu}$	discrete ordinate vector
σ	Stefan-Boltzmann constant
$\boldsymbol{\phi}$	(thermodynamic) state
Ω	solid angle

Subscripts and superscripts

b	blackbody
E	with respect to the energy equation
fit	fitted-mean
FSCK	with respect to the FSCK model
G	with respect to the incident radiation
gas	gas
GL	with respect to the Gauss-Legendre method
i	index
j	index for forward and backward directions
k	index for pseudo-bands
l	index for discrete ordinates
m	index
max	maximum
mean	mean
min	minimum
mix	mixture
n	index for nodes
p	pressure-based
P	Planck-averaged
q	with respect to the radiation wall heat flux
R	Rosseland-mean
rad	radiation
ref	reference
s	surface
S	with respect to the radiation heat source term
soot	soot
tot	total
v	volume
wall	wall
WSGG	WSGG-mean
η	spectral
$'$	auxiliary

Acronyms

1D	one-dimensional
2D	two-dimensional
3D	three-dimensional
ALBDF	absorption line blackbody distribution function
ARD	absolute relative deviation
B	band approach
bioliq EFG	bioliq Entrained Flow Gasifier
CFD	computational fluid dynamics
DB	domain-based
DO	discrete ordinates
DOM	discrete ordinates model
FSCK	full-spectrum correlated-k distribution
FSCKM	full-spectrum correlated-k distribution model
GG	grey-gas
GGM	grey-gas model
LBL	line-by-line
LBLM	line-by-line model
MBL	mean beam length approach
N	numerical solution approach
NGG	non-grey-gas
NGGM	non-grey-gas model
P1M	P-1 model
RANS	Reynolds averaged Navier-Stokes
RD	relative deviation
REGA	atmospheric Research Entrained flow GAsifier
SIMPLEC	semi-implicit method for pressure linked equations-consistent
SLWSGG	spectral-line-weighted-sum-of-grey-gas
SLWSGGM	spectral-line-weighted-sum-of-grey-gas model
T	tabulated approach with 21 cross-sections
T-32	tabulated approach with 32 cross-sections
T-6	tabulated approach with 6 cross-sections
UD	user-defined
WSGG	weighted-sum-of-grey-gas
WSGGM	weighted-sum-of-grey-gas model

described using the domain-based model [29]. This is an available model in ANSYS Fluent [30] that relies on the weighted-sum-of-grey-gas (WSSG) model of Smith et al. [31] (originally developed for atmospheric combustion conditions), the scaling rules of Edwards and Matavosian [32] and the mean beam length model of Hottel and Sarofim [33].

More recent developments based on spectral-line-weighted-sum-of-grey-gas (SLWSGG) models (for example, see [34,35]), full-spectrum correlated-k distribution (FSCK) models (for example, see [36–38]) or improved WSGG models (for example, see [39–43]) were not applied since substantial efforts are required for their coupling with CFD. In contrast to older models developed using either measured narrow-band transmissivities or narrow-band and/or wide-band models, such modern developments are typically based on appropriate line-by-line (LBL) calculations, which are performed using the available spectroscopic databases as HITEMP-2010 [44] and using one of the common line-shape functions as the Lorentz function or the Voigt function.

Transmissivity spectra, corresponding to such calculated absorption spectra, are mainly in very good agreement with the measured spectra at atmospheric conditions. However, at high-density conditions, the absorption coefficients in the line wings are overestimated due to imperfections of the line-shape functions. In order to minimise the discrepancies, Hartmann et al. [45–47], Pearson et al. [34,35], Westlye et al. [48] and Alberti et al. [49–54] developed empirical correction methods. Hartmann et al. [45–47] tabulated χ-factors for specific temperature and wavenumber ranges. Pearson et al. [34,35] cut off the H_2O lines after 2750 half-widths and the CO_2 and CO lines after 600 half-widths. Westlye et al. [48] tested the pseudo-Lorentz line-shape function. Alberti et al. [49,50,52–54] suggested cut-off criteria that take temperature and total pressure into account and are applicable for a wide range of temperatures and total pressures. The latter criteria were recently used to re-create emissivity charts [49–51,53,54] and to develop customised WSGG models for atmospheric and high-pressure entrained flow gasification processes [2,6]. The models were applied in RANS based CFD simulations which demonstrated again the dominant influence of thermal radiation on the heat removal [2,6,7]. Possible simplifications were suggested for atmospheric conditions [2]. However, reference analyses with advanced gas radiation property models including the LBL model were carried out neither for atmospheric nor for high-pressure conditions.

Therefore, this study analyses the effects of advanced and simplified gas radiation property models on the radiation predictions at atmospheric and high-pressure entrained flow gasification conditions. In order to provide recommendations for the selection of gas radiation property models to be incorporated into CFD models for entrained flow gasification processes, one-dimensional radiation simulations for slab configurations were connected with two-dimensional CFD simulations.

The experiments and the methods used for the investigation are described in Section 2 and Section 3, respectively. The results of the simulations are presented and discussed in Section 4. The conclusions are summarised in Section 5.

2. Experiments

This section briefly introduces the atmospheric and high-pressure entrained flow gasification experiments considered in the 1D slab simulations and in the CFD simulations. The 1D slab simulations were performed with respect to the atmospheric Research Entrained flow GAsifier (REGA) of Karlsruhe Institute of Technology and to the bioliq Entrained Flow Gasifier (bioliq EFG) while the CFD simulations focussed on the bioliq EFG only, as the CFD models and predictions regarding REGA are reported elsewhere [2,7].

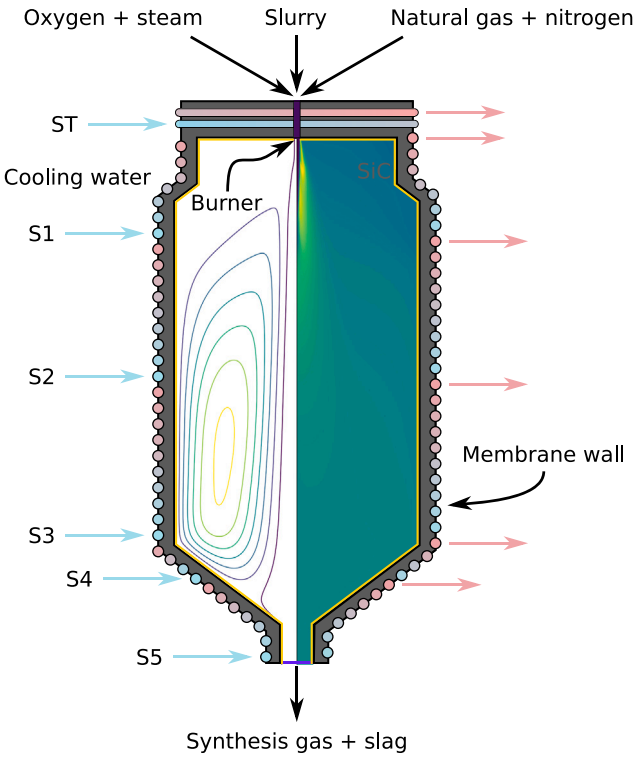

Fig. 1. Schematic cross-section of the bioliq EFG reactor with the cooling circuits S1, ..., S5 and ST.

2.1. REGA

The REGA is an atmospheric laboratory-scale entrained flow gasifier with a cylindrical geometry and a laterally heated wall and is applied for the gasification of carbonaceous liquid and suspension fuels using oxygen-enriched air [7,55].

The 1D slab simulations relied on recent CFD predictions of two REGA experiments considering the gasification of ethylene glycol [3,4,7], the REGA experiments TUC3 V786 and TUC5 V1105, deviating in stoichiometric ratio and adiabatic temperature (see [3,4,7]).

2.2. bioliq EFG

The bioliq EFG is the high-pressure entrained flow gasifier of the bioliq pilot plant and is used for the production of synthesis gas from biogenic and anthropogenic fuels [1,56]. Oxygen and steam are fed as gasification media while natural gas and nitrogen are applied for ignition and flame stabilisation and for purging, respectively [56]. The cross-section of the inner reactor chamber is shown in Fig. 1. Accordingly, the bioliq EFG is equipped with a segmental cooling screen and a refractory made of SiC. Six water cooling circuits are used for the main heat removal from the bioliq EFG while two further water cooling circuits are applied for the cooling of the main burner and the auxiliary burner. During operation, solid particles and liquid droplets, containing mainly mineral compounds, deposit on the refractory and form liquid, crystalline and solidified slag layers [56] while only the molten slag flows down the refractory and leaves the inner reactor chamber together with the synthesis gas [56].

The 1D slab simulations and the CFD simulations of the bioliq EFG focussed on the bioliq EFG experiment V82.1 [5], in which a model slurry consisting of 96% ethylene glycol and 4% glass beads (in mass fractions) was gasified using oxygen and steam at a total gas pressure of 40 bar and a total thermal input of 4 MW [5]. Mass or volume flow rates, temperatures and pressures of the inlet streams and the dry gas

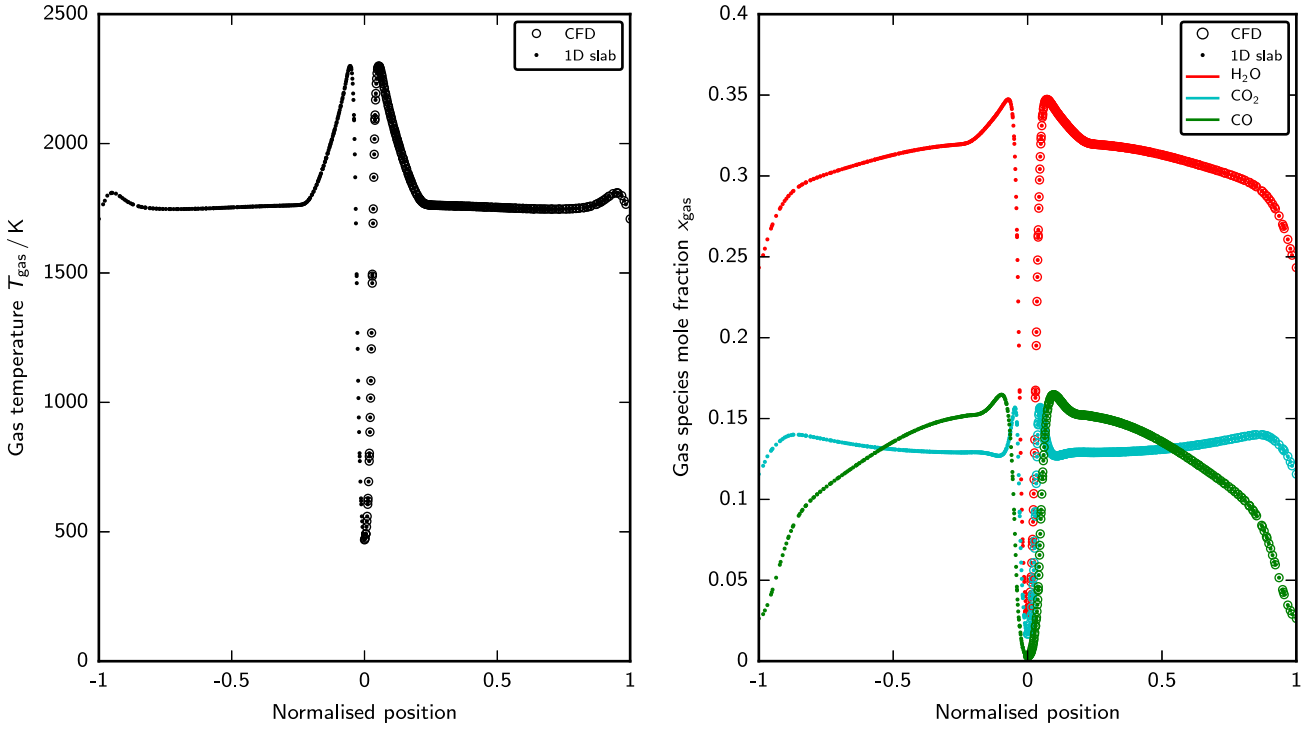

Fig. 2. Predicted gas temperature (left) and gas species mole fractions (right) profiles for the REGA experiment TUC3 V786 at the nozzle distance of 100 mm.

species concentrations after the quench were recorded during operation and were the basis for elemental and energy balances and for equilibrium calculations [5]. The process calculations provided the input data for the CFD model and the segmental heat removal [5]. Within this study, the latter is used as experimental basis for comparison with the predictions.

3. Methods

This section describes the methods that were applied (i) to perform the 1D slab simulations, the CFD simulations and the LBL calculations, (ii) to generate the emissivity charts and the WSGG models and (iii) to incorporate GG models, SLWSGG models, FSCK models and soot contributions into the 1D slab model.

3.1. 1D slab simulations

1D slab simulations are concerned with the radiative heat transfer between two infinite parallel plates and are regularly used for comparison of gas radiation property models (for example, see [34,35,57–59]). The plates with the wall temperatures T_{wall} and the wall emissivities $\epsilon_{wall} = 0.8$ are separated from each other by the distance L. Mass, momentum, energy and species balance equations are not solved within these simulations. Instead, one-dimensional profiles are assumed for gas temperature, gas pressure and gas species concentrations. The profiles, used within this study, were obtained from the CFD predictions for the REGA experiments TUC3 V786 and TUC5 V1105 (see [7]) at nozzle distances of 100 mm and 300 mm and from the CFD predictions for the bioliq EFG experiment V82.1 (with the user-defined WSGG model and the band approach; see Section 3.2) at nozzle distances of 260 mm and 1524 mm. The extracted gas temperature profiles and the gas species mole fractions profiles of H_2O, CO_2 and CO are shown as open circle markers in Figs. 2–7 and were mirrored for the 1D slab simulations. Additionally, further profiles were defined to investigate uncertainties related to the bioliq EFG experiment (see Section 4.4).

Following the definition of the profiles, absorption spectra were determined using LBL calculations (see Section 3.3). These spectra provided the most accurate gas radiation property model and the reference model within this study. Additionally, grey-gas (GG) and non-grey-gas (NGG) models were prepared using absorption coefficients and weights that were provided by user-defined WSGG models (see Section 3.5), by the domain-based model (see Section 3.6.2), by user-defined GG models (see Sections 3.6.3 and 3.6.4), by the latest absorption line blackbody distribution function (ALBDF) tables for SLWSGG models (see Section 3.7) and by the latest FSCK tables for FSCK models (see Section 3.8).[2]

In the 1D slab simulations, the grey-gas absorption coefficients K_{gas} or the non-grey-gas absorption coefficients $\boldsymbol{K}_{gas} = (K_{gas,k})$ were combined with the soot absorption coefficient K_{soot} (see Section 3.9). The (total) absorption coefficients, that were finally applied in the radiative heat transfer simulations using the discrete ordinates (DO) model or the P-1 model, are given by

$$K = K_{gas} + K_{soot}\,, \tag{1}$$

$$K_k = K_{gas,k} + K_{soot}\,, \tag{2}$$

where K is the (total) absorption coefficient and K_k is the (total) absorption coefficient of discrete wavenumber or pseudo-band k.

3.1.1. 1D slab simulations using the DO model

1D slab simulations using the DO model (see [58,60]) were performed by solving radiative transfer equations for intensities I or spectral intensities I_η in 36 forward and 36 backward directions under application of different gas radiation property models.

[2] For simplicity, the predictions based on the different gas radiation property models are hereinafter referred to the underlying models (i. e. LBL, WSGG, GG, SLWSGG and FSCK models).

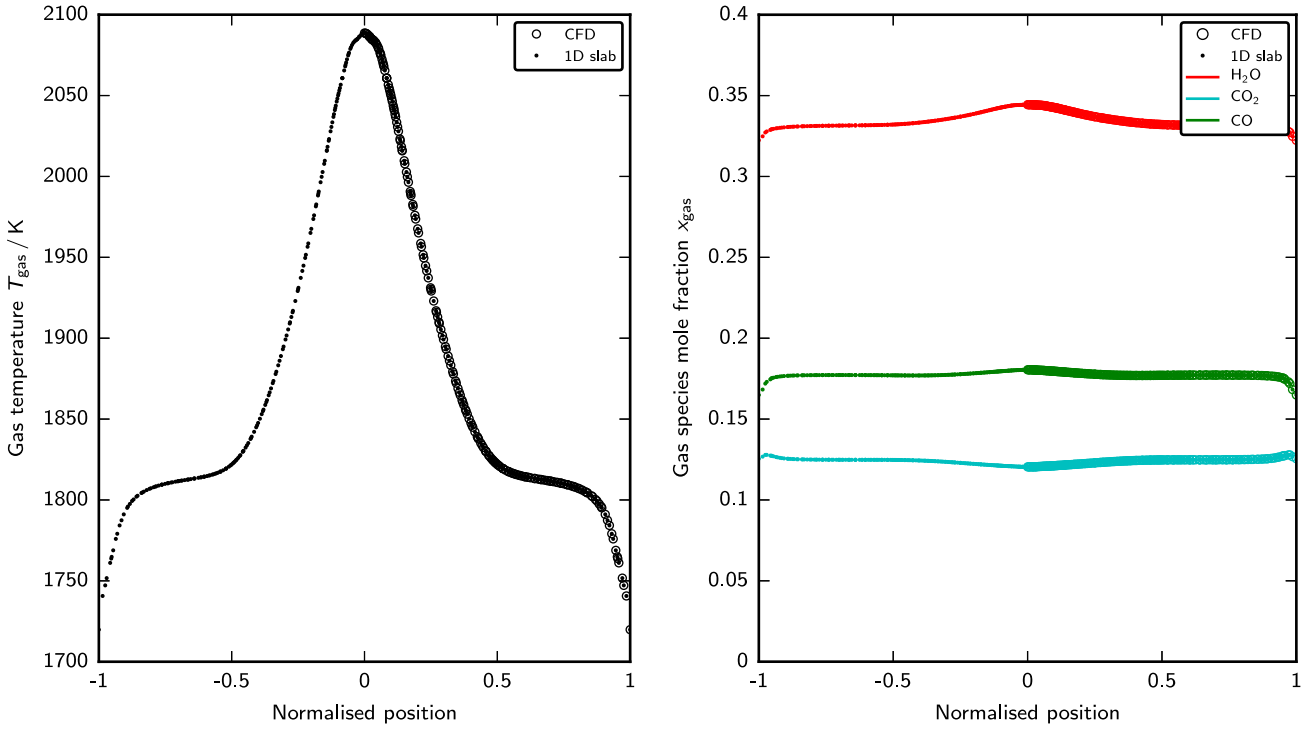

Fig. 3. Predicted gas temperature (left) and gas species mole fractions (right) profiles for the REGA experiment TUC3 V786 at the nozzle distance of 300 mm.

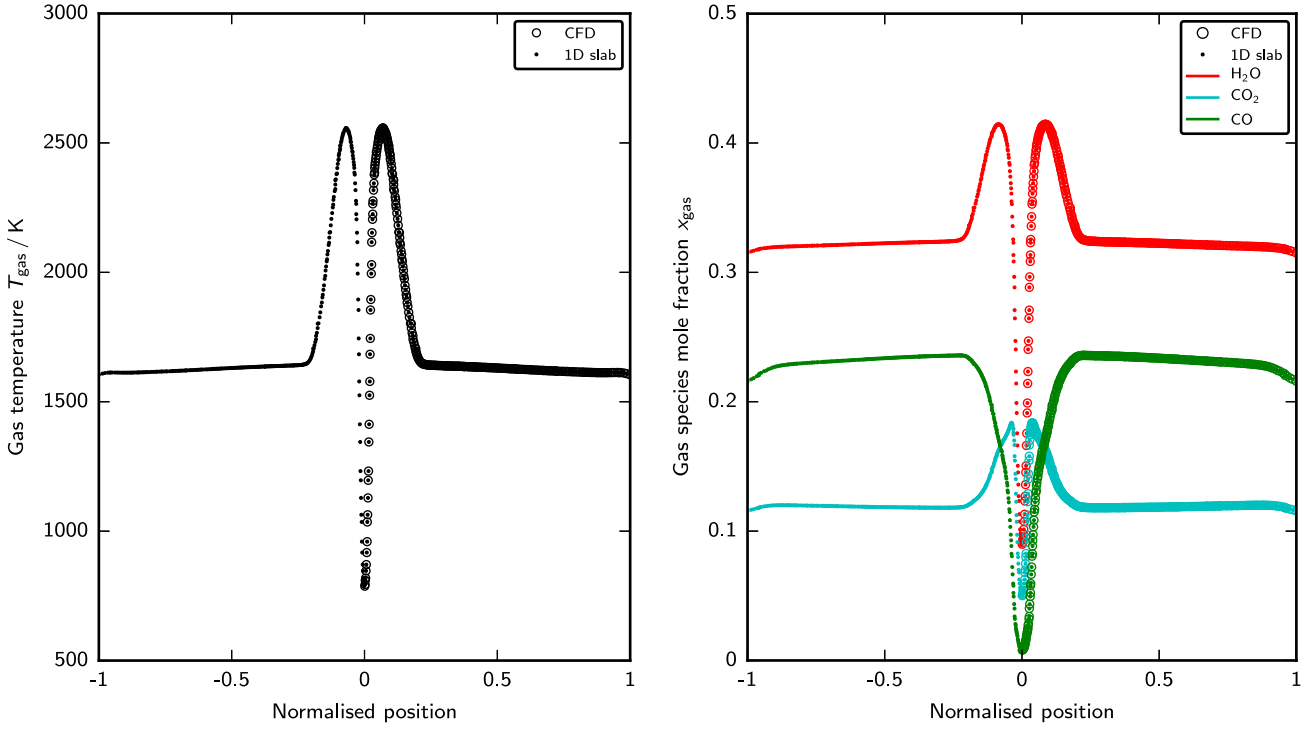

Fig. 4. Predicted gas temperature (left) and gas species mole fraction (right) profiles for the REGA experiment TUC5 V1105 at the nozzle distance of 100 mm.

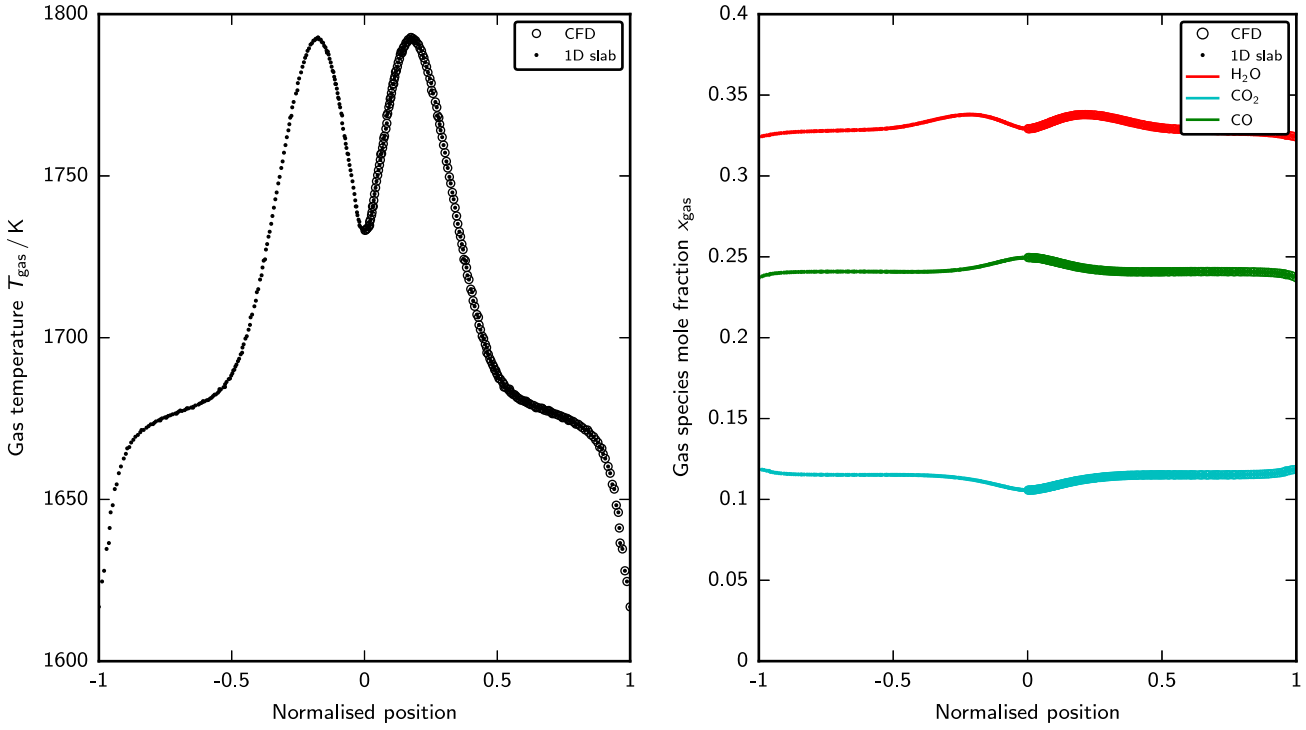

Fig. 5. Predicted gas temperature (left) and gas species mole fractions (right) profiles for the REGA experiment TUC5 V1105 at the nozzle distance of 300 mm.

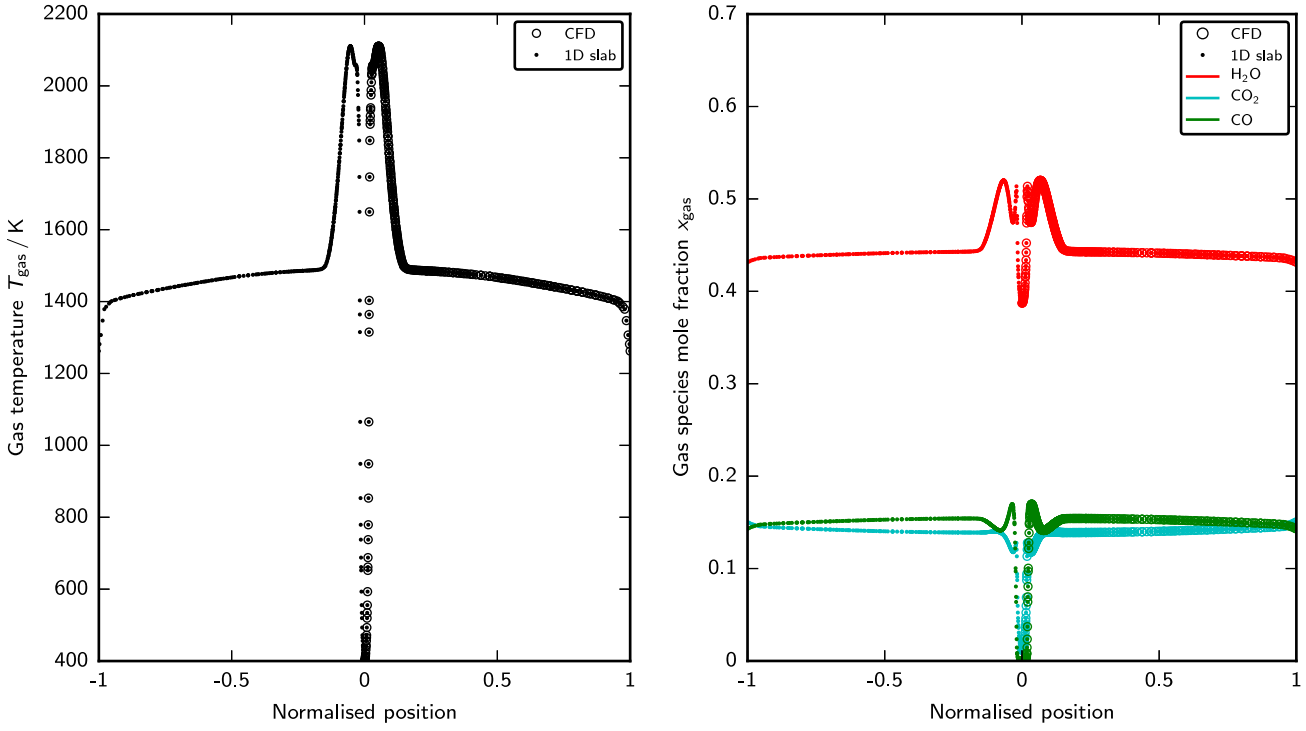

Fig. 6. Predicted gas temperature (left) and gas species mole fractions (right) profiles for the bioliq EFG experiment V82.1 at the nozzle distance of 260 mm.

The radiative transfer equation and the boundary conditions for the application with GG models are given by

$$\frac{\mathrm{d}I}{\mathrm{d}z} + K\,I = K\,\frac{\sigma\,T^4}{\pi}\,, \tag{3}$$

$$I|_{\mathrm{wall}} = \varepsilon_{\mathrm{wall}}\,\frac{\sigma\,T_{\mathrm{wall}}^4}{\pi} + \frac{1-\varepsilon_{\mathrm{wall}}}{\pi}\int_{\Omega_{\mathrm{wall}}} I\,\mathrm{d}\Omega\,, \tag{4}$$

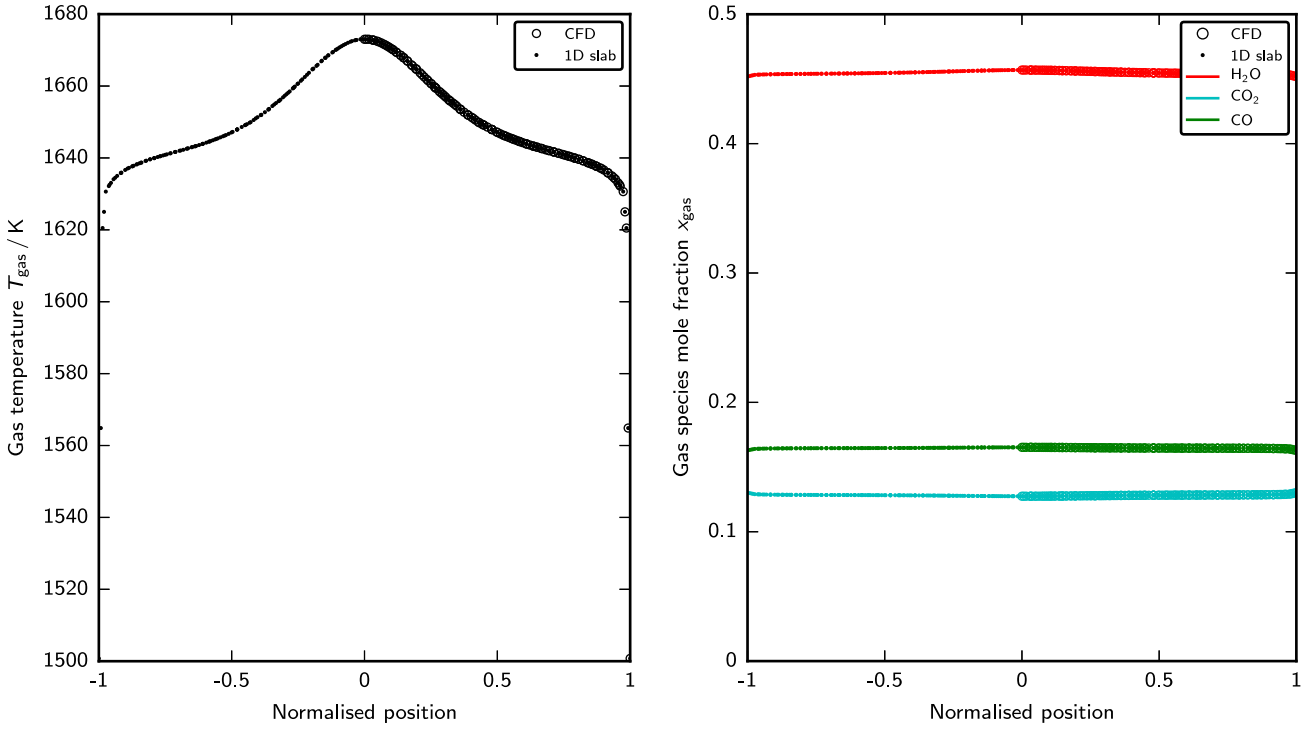

Fig. 7. Predicted gas temperature (left) and gas species mole fraction (right) profiles for the bioliq EFG experiment V82.1 at the nozzle distance of 1524 mm.

where I is the intensity, z is the position, K is the absorption coefficient, σ is the Stefan–Boltzmann constant, T is the temperature and Ω is the solid angle.

The radiative transfer equation and the boundary conditions for the connection with absorption spectra are defined by

$$\frac{\mathrm{d}I_{\eta,k}}{\mathrm{d}z} + K_k\, I_{\eta,k} = K_k\, \frac{\dot{e}_{\eta,\mathrm{b}}\left(\eta_k, T\right)}{\pi}\,, \tag{5}$$

$$I_{\eta,k}\big|_{\mathrm{wall}} = \varepsilon_{\mathrm{wall}}\, \frac{\dot{e}_{\eta,\mathrm{b}}\left(\eta_k, T_{\mathrm{wall}}\right)}{\pi} + \frac{1-\varepsilon_{\mathrm{wall}}}{\pi} \int_{\Omega_{\mathrm{wall}}} I_\eta\, \mathrm{d}\Omega\,, \tag{6}$$

where $I_{\eta,k}$ is the spectral intensity of discrete wavenumber k, K_k is the absorption coefficient of discrete wavenumber k and $\dot{e}_{\eta,\mathrm{b}}$ is the Planck function.

The radiative transfer equation and the boundary conditions for the incorporation of pseudo-band models are given by

$$\frac{\mathrm{d}I_k}{\mathrm{d}z} + K_k\, I_k = K_k\, a_k\left(T\right)\, \frac{\sigma\, T^4}{\pi}\,, \tag{7}$$

$$I_k|_{\mathrm{wall}} = \varepsilon_{\mathrm{wall}}\, a_k\left(T_{\mathrm{wall}}\right)\, \frac{\sigma\, T_{\mathrm{wall}}^4}{\pi} + \frac{1-\varepsilon_{\mathrm{wall}}}{\pi} \int_{\Omega_{\mathrm{wall}}} I\, \mathrm{d}\Omega\,, \tag{8}$$

where I_k is the intensity, K_k is the absorption coefficient and a_k is the weight, each of pseudo-band k.

1D slab simulations using the DO model provided total, spectral or band intensities in the forward and in the backward directions for each discrete ordinate l, $l = 1, \ldots, 36$. Total intensities were obtained with application of GG models while spectral or band intensities were determined with application of NGG models. Corresponding total intensities I_l^j, $j = +, -$, were subsequently determined by

$$I_l^j = \begin{cases} \sum_k I_{\eta,k,l}^j\, \Delta\eta_k\,, & \text{if relying on LBL models} \\ \sum_k I_{k,l}^j\,, & \text{if relying on WSGG or SLWSGG models} \\ \sum_k w_{\mathrm{FSCK},k}\, I_{k,l}^j\,, & \text{if relying on FSCK models} \end{cases}, \tag{9}$$

where $\Delta\eta_k$ is the wavenumber width of discrete wavenumber k and $\boldsymbol{w}_{\mathrm{FSCK}} = \left(w_{\mathrm{FSCK},k}\right)$ are the quadrature weights as originally used for the generation of the FSCK tables (see Section 3.8). The total intensities were used to determine the total incident radiation G, the total radiation heat flux $\dot{q}_{\mathrm{rad}}$ and the total radiation heat source term $S_{\mathrm{E,rad}}$.

The total incident radiation G and the total radiation heat flux $\dot{q}_{\mathrm{rad}}$ are given by

$$G = 2\,\pi \sum_l w_{\mathrm{GL},l}\, \left(I_l^+ + I_l^-\right)\,, \tag{10}$$

$$\dot{q}_{\mathrm{rad}} = 2\,\pi \sum_l \mu_l\, w_{\mathrm{GL},l}\, \left(I_l^+ - I_l^-\right)\,, \tag{11}$$

where $w_{\mathrm{GL},l}$ is the quadrature weight, μ_l is the discrete ordinate, I_l^+, is the total intensity in forward direction and I_l^- is the total intensity in backward direction, each for the discrete ordinate l. Quadrature weights $\boldsymbol{w}_{\mathrm{GL}} = \left(w_{\mathrm{GL},l}\right)$ and discrete ordinates $\boldsymbol{\mu} = \left(\mu_l\right)$ were obtained from the Gauss–Legendre quadrature weights and nodes [61]. The total radiation heat source term $S_{\mathrm{E,rad}}$ is defined by the negative derivative of the total radiation heat flux $\dot{q}_{\mathrm{rad}}$.

3.1.2. 1D slab simulations using the P-1 model

1D slab simulations using the P-1 model (see [58]) were solved with Marshak boundary conditions. With application of GG models, the incident radiation G was determined by

$$\frac{\mathrm{d}}{\mathrm{d}z}\left(\frac{1}{3\,K}\,\frac{\mathrm{d}G}{\mathrm{d}z}\right) - K\,G = -4\,K\,\sigma\,T^4\,, \tag{12}$$

$$\frac{1}{3\,K}\,\left\langle \nabla G, \boldsymbol{n}\right\rangle|_{\mathrm{wall}} = \frac{\varepsilon_{\mathrm{wall}}}{2\left(2-\varepsilon_{\mathrm{wall}}\right)}\left(4\,\sigma T_{\mathrm{wall}}^4 - G|_{\mathrm{wall}}\right)\,, \tag{13}$$

where $\boldsymbol{n}$ is the normal vector. The radiation heat flux $\dot{q}_{\mathrm{rad}}$ and the radiation heat source term $S_{\mathrm{E,rad}}$ were subsequently obtained by

$$\dot{q}_{\mathrm{rad}} = -\frac{1}{3\,K}\,\frac{\mathrm{d}G}{\mathrm{d}z}\,, \tag{14}$$

$$S_{\mathrm{E,rad}} = K\,G - 4\,K\,\sigma\,T^4\,. \tag{15}$$

The P-1 approximation and the boundary conditions on spectral basis were applied as

$$\frac{\mathrm{d}}{\mathrm{d}z}\left(\frac{1}{3\,K_k}\,\frac{\mathrm{d}G_{\eta,k}}{\mathrm{d}z}\right) - K_k\,G_{\eta,k} = -4\,K_k\,\dot{e}_{\eta,\mathrm{b}}\left(\eta_k, T\right)\,, \tag{16}$$

$$\frac{1}{3\,K_k}\,\langle\nabla G_{\eta,k}, \boldsymbol{n}\rangle\Big|_{\mathrm{wall}} = \frac{\varepsilon_{\mathrm{wall}}}{2\left(2-\varepsilon_{\mathrm{wall}}\right)}\left(4\,\dot{e}_{\eta,\mathrm{b}}\left(\eta_k, T_{\mathrm{wall}}\right) - G_{\eta,k}\Big|_{\mathrm{wall}}\right)\,, \tag{17}$$

where $G_{\eta,k}$ is the spectral incident radiation of discrete wavenumber k. The spectral radiation heat flux $\dot{q}_{\mathrm{rad},\eta,k}$ and the spectral radiation heat source term $S_{\mathrm{E,rad},\eta,k}$, each of discrete wavenumber k, were subsequently determined by

$$\dot{q}_{\mathrm{rad},\eta,k} = -\frac{1}{3\,K_k}\,\frac{\mathrm{d}G_{\eta,k}}{\mathrm{d}z}\,, \tag{18}$$

$$S_{\mathrm{E,rad},\eta,k} = K_k\,G_{\eta,k} - 4\,K_k\,\dot{e}_{\eta,\mathrm{b}}\left(\eta_k, T\right)\,. \tag{19}$$

The total incident radiation G, the total radiation heat flux $\dot{q}_{\mathrm{rad}}$ and the total radiation heat source term $S_{\mathrm{E,rad}}$ were finally calculated by

$$G = \sum_k G_{\eta,k}\,\Delta\eta_k\,, \tag{20}$$

$$\dot{q}_{\mathrm{rad}} = \sum_k \dot{q}_{\mathrm{rad},\eta,k}\,\Delta\eta_k\,, \tag{21}$$

$$S_{\mathrm{E,rad}} = \sum_k S_{\mathrm{E,rad},\eta,k}\,\Delta\eta_k\,. \tag{22}$$

The P-1 approximation and the boundary conditions on pseudo-band basis were used as

$$\frac{\mathrm{d}}{\mathrm{d}z}\left(\frac{1}{3\,K_k}\,\frac{\mathrm{d}G_k}{\mathrm{d}z}\right) - K_k\,G_k = -4\,K_k\,a_k\,(T)\,\sigma\,T^4\,, \tag{23}$$

$$\frac{1}{3\,K_k}\,\langle\nabla G_k, \boldsymbol{n}\rangle|_{\mathrm{wall}} = \frac{\varepsilon_{\mathrm{wall}}}{2\left(2-\varepsilon_{\mathrm{wall}}\right)}\left(4\,a_k\left(T_{\mathrm{wall}}\right)\,\sigma T_{\mathrm{wall}}^4 - G_k|_{\mathrm{wall}}\right)\,, \tag{24}$$

where G_k is the incident radiation of pseudo-band k. The radiation heat flux $\dot{q}_{\mathrm{rad},k}$ and the radiation heat source term $S_{\mathrm{E,rad},k}$, each of pseudo-band k, were subsequently calculated by

$$\dot{q}_{\mathrm{rad},k} = -\frac{1}{3\,K_k}\,\frac{\mathrm{d}G_k}{\mathrm{d}z}\,, \tag{25}$$

$$S_{\mathrm{E,rad},k} = K_k\,G_k - 4\,K_k\,a_k\,\sigma\,T^4\,. \tag{26}$$

The total incident radiation G, the total radiation heat flux $\dot{q}_{\mathrm{rad}}$ and the total radiation heat source term $S_{\mathrm{E,rad}}$ were finally determined by

$$G = \begin{cases} \sum_k G_k\,, & \text{if relying on WSGG or SLWSGG models} \\ \sum_k w_{\mathrm{FSCK},k}\,G_k\,, & \text{if relying on FSCK models} \end{cases}\,, \tag{27}$$

$$\dot{q}_{\mathrm{rad}} = \begin{cases} \sum_k \dot{q}_{\mathrm{rad},k}\,, & \text{if relying on WSGG or SLWSGG models} \\ \sum_k w_{\mathrm{FSCK},k}\,\dot{q}_{\mathrm{rad},k}\,, & \text{if relying on FSCK models} \end{cases}\,, \tag{28}$$

$$S_{\mathrm{E,rad}} = \begin{cases} \sum_k S_{\mathrm{E,rad},k}\,, & \text{if relying on WSGG or SLWSGG models} \\ \sum_k w_{\mathrm{FSCK},k}\,S_{\mathrm{E,rad},k}\,, & \text{if relying on FSCK models} \end{cases}\,. \tag{29}$$

3.1.3. Relative deviations

Results of the 1D slab simulations are compared in this study using absolute relative deviations (ARD) which are defined by

$$\mathrm{ARD_q} = \frac{\left|\,\dot{q}_{\mathrm{rad,wall}}\Big|_X - \dot{q}_{\mathrm{rad,wall}}\Big|_Y\,\right|}{\left|\,\dot{q}_{\mathrm{rad,wall}}\Big|_Y\,\right|}\,, \tag{30}$$

$$\mathrm{ARD_S} = \frac{\int_z\left|\,S_{\mathrm{E,rad}}\Big|_X - S_{\mathrm{E,rad}}\Big|_Y\,\right|\mathrm{d}z}{\int_z\left|\,S_{\mathrm{E,rad}}\Big|_Y\,\right|\mathrm{d}z}\,, \tag{31}$$

$$\mathrm{ARD_G} = \frac{1}{\sum_n 1}\sum_n \frac{\left|\,G_n|_X - G_n|_Y\,\right|}{\left|\,G_n|_Y\,\right|}\,, \tag{32}$$

where X refers to the predictions which are to be evaluated and Y refers either to the reference or to the baseline predictions. Thus, the absolute relative deviation with respect to the heat source term $\mathrm{ARD_S}$ is defined as global integral relative deviation while the absolute relative deviation with respect to the incident radiation $\mathrm{ARD_G}$ is a node-averaged relative deviation.

The reference and the baseline predictions, with a few exceptions, are based on the DO model and the LBL model as the absorption spectra provide the most accurate gas radiation property model (see Section 3.1). Furthermore, the reference predictions in Sections 4.1 and 4.2 are always based on the extracted and mirrored profiles while modified profiles were used for the baseline predictions in context with the sensitivity analyses in Section 4.4.

3.2. CFD simulations

CFD simulations within this study focussed on the bioliq EFG experiment V82.1 and were performed using the CFD model of the bioliq EFG, that has been developed using ANSYS Fluent [30] and user-defined functions[3] for steady-state design and scale-up simulations. Following the preceding CFD model [6], the gas phase is described using the RANS approach in the Eulerian specification of reference. Favre averaged Navier–Stokes equations, Favre averaged species balance equations and the turbulence equations of the standard $k-\epsilon$ model [62,63] are solved on an axisymmetric two-dimensional computing domain with $2.2 \cdot 10^5$ cells using the finite-volume method and the SIMPLEC algorithm [64]. The second-order upwind scheme is applied for the discretisation of the momentum and energy equations while the turbulence and pressure equations are discretised using the first-order upwind scheme and the PRESTO! scheme, respectively. The gas reactions are described using the eddy-dissipation-concept model [65] and a global reaction mechanism while the discrete ordinates model is combined with one of three different gas radiation property models to account for radiation: (i) a NGG model with six pseudo-bands and with weighting factors and absorption coefficients from the user-defined WSGG model (see Section 3.5.2) or (ii) a GG model with absorption coefficients from the user-defined WSGG model (see Section 3.5.2) and the mean beam length model (see Section 3.6.1) or (iii) the domain-based model (see Section 3.6.2). The radiative transfer equations are solved for 256 directions (8 × 8 directions in each of the four octants) and each pseudo-band using the finite-volume method [66,67] and the first-order upwind scheme.

The dispersed phase is injected using particles consisting of liquid and solid fractions. The liquid fractions contain ethylene glycol which vaporises according to the classical convective vaporisation model, while the solid glass beads fractions are considered as inert (with respect to chemical reactions and phase transformations) and mainly deposit as slag on the wall boundary. Radiative heat transfer to the slurry droplets and solid glass beads is simplified assuming opaque and grey particle surfaces.

The slag phase is described using simplified slag flow equations following the slag flow model of Seggiani [68]. The surfaces of both the refractory and the slag phase are treated as opaque and grey.

[3] Particularly, the macros DEFINE_EMISSIVITY_WEIGHTING_FACTOR and DEFINE_GRAY_BAND_ABS_COEFF are used to incorporate the weights and the gas absorption coefficients based on the user-defined WSGG model, while the macro DEFINE_WSGGM_ABS_COEFF is applied for the gas absorption coefficient based on the user-defined WSGG model and the mean beam length model (see Section 3.6.1). Note that the macro DEFINE_WSGGM_ABS_COEFF should only be applied in combination with the mean beam length approach.

3.3. LBL calculations

LBL calculations were performed using the HITEMP-2010 databases for H_2O, CO_2 and CO [44] and the LBL software of Alberti et al. [49–51,53,54] to obtain gas absorption spectra for specified total gas pressures p_{gas}, gas temperatures T_{gas} and gas species mole fractions $\boldsymbol{x}_{gas}$ with a spectral wavenumber range between $\eta_{min} = 0$ and $\eta_{max} = 30000\ cm^{-1}$. The HITEMP-2010 databases provided the parameters at the reference pressure of 1 atm and the reference temperature of 296 K for the numerous absorption lines of each species including the line position, the integrated line intensity and the half-widths of the line for self-broadening and foreign-broadening. The spectral absorption coefficient of each line was described using the Voigt function as line-shape function to a minimum absorption coefficient of $10^{-9}\ cm^{-1}$ following previous descriptions [54]. This also included the application of the empirical cut-off criteria

$$n_{CO_2}(p_{gas}, T_{gas}) = 429.99 \cdot \left(\frac{T_{gas}}{296\ K} \frac{1\ bar}{p_{gas}} \right)^{0.822}, \tag{33}$$

$$n_{H_2O}(p_{gas}, T_{gas}) = n_{CO}(p_{gas}, T_{gas}) = 686.65 \cdot \left(\frac{T_{gas}}{296\ K} \frac{1\ bar}{p_{gas}} \right)^{0.833} \tag{34}$$

to correct the overestimation of the absorption in the line wings of each line [54]. Each criterion estimates the number of half-width n away from the line centre above which each line is to be cut [54]. The gas absorption spectrum was finally determined from the absorption contributions of each line and each species [54].

3.4. Emissivity charts

Emissivity charts for specified total gas pressures p_{gas} and gas species mole fractions $\boldsymbol{x}_{gas}$ were created each using 45 absorption spectra obtained at 300 K, 350 K, …, 1950 K, 2000 K, 2100 K, …, 3000 K and using 30 pressure path lengths defined by logarithmic spacing between 0.001 bar cm and 6000 bar cm. The total gas emissivity $\varepsilon_{gas,tot}$ was calculated by

$$\varepsilon_{gas,tot} = \frac{\int_{\eta_{min}}^{\eta_{max}} \varepsilon_{gas,\eta}\, \dot{e}_{\eta,b}(\eta, T)\, d\eta}{\int_{\eta_{min}}^{\eta_{max}} \dot{e}_{\eta,b}(\eta, T)\, d\eta}, \tag{35}$$

where $\varepsilon_{gas,\eta}$ is the spectral gas emissivity and $\dot{e}_{\eta,b}$ is the Planck function. The spectral gas emissivity $\varepsilon_{gas,\eta}$ is defined by

$$\varepsilon_{gas,\eta} = 1 - \exp\left(-K_{gas}\, L\right), \tag{36}$$

where K_{gas} is the gas absorption coefficient (as determined by the LBL calculations) and L is the path length.

3.5. WSGG models

The WSGG models applied in this study were the model of Smith et al. [31], the user-defined model for the REGA conditions (see Section 3.5.1) and the user-defined model for the bioliq EFG conditions (see Section 3.5.2).

The WSGG model of Smith et al. [31] was originally generated using the exponential-wide-band model of Edwards and Modak [69,70] for H_2O-CO_2-N_2 mixtures at a total gas pressure p_{gas} of 1 atm and at gas temperatures T_{gas} between 600 K and 2400 K and with focus on several atmospheric combustion conditions ($p_{CO_2,gas} = 0$, $p_{H_2O,gas} = 0$, $p_{CO_2,gas} = 1$ atm, $p_{H_2O,gas}/p_{CO_2,gas} = 1$, $p_{H_2O,gas}/p_{CO_2,gas} = 2$). In this study, the model was considered due to its popularity and its implementation in the domain-based model of ANSYS Fluent [30] and was only used in this context (see Section 3.6.2).

The user-defined WSGG models were obtained by constrained non-linear multi-variable regressions of the corresponding total emissivity charts using the *fmincon* method of Matlab [71] and the expression

$$\varepsilon_{gas,tot} = \sum_k a_k(T) \left(1 - \exp\left(-K_{gas,k}\, L\right)\right) \tag{37}$$

where a_k is the weight of pseudo-band k, $K_{gas,k}$ is the gas absorption coefficient of pseudo-band k and L is the path length. The weight a_k is described by a polynomial while the gas absorption coefficient $K_{gas,k}$ is defined by

$$K_{gas,k} = K_{p,gas,k} \left(x_{H_2O,gas} + x_{CO_2,gas}\right) p_{gas}, \tag{38}$$

where $K_{p,gas,k}$ is the pressure-based gas absorption coefficient of pseudo-band k, $x_{H_2O,gas}$ is the gas species mole fraction of H_2O, $x_{CO_2,gas}$ is the gas species mole fraction of CO_2 and p_{gas} is the total gas pressure. The above expression does not include the gas species mole fraction of CO since improved fitting results can be obtained without considering the gas species mole fraction of CO.[4] The reason is that, although there is a relatively large amount of CO present in the gas phase, its contribution to the total gas emissivity $\varepsilon_{gas,tot}$ is relatively weak due to strong overlapping of the 4.7 μm band of CO with the 6.3 μm band of H_2O and the 4.3 μm band of CO_2.

The user-defined WSGG models were coupled with the respective radiation model using two different approaches: the band approach and the mean beam length approach. The band approach assumes pseudo-bands in the radiation simulations with the weights and the gas absorption coefficients evaluated at the local gas conditions while the mean beam length approach is actually a grey-gas approach (see Section 3.6.1).

3.5.1. User-defined WSGG model for REGA conditions

The user-defined WSGG model for the REGA conditions was developed in the preceding study [2]. After an elaborative analysis of gas conditions and emissivities, emissivity charts were generated for 13 gas conditions, for which gas species mole fractions of CO and H_2O were assumed to be 0.18 and 0.33 while the gas species mole fractions of CO_2 were varied corresponding to gas species mole fraction ratios of H_2O and CO_2 between 1.5 and 3.3 [2]. The WSGG model was finally established using the emissivity charts for the 13 gas conditions, a minimum fit temperature of 450 K, a maximum fit temperature of 2950 K, six pseudo-bands and polynomials of sixth order.

3.5.2. User-defined WSGG model for bioliq EFG conditions

The user-defined WSGG model for the bioliq EFG conditions was determined based on preceding CFD simulations of the bioliq EFG experiment V82.1. Since the predicted approximately uniform gas species concentrations of H_2O, CO_2 and CO were similar to the equilibrium gas species concentrations, the WSGG model was generated using the emissivity chart for the equilibrium gas condition in combination with a minimum fit temperature of 450 K, a maximum fit temperature of 3000 K, six pseudo-bands and polynomials of fourth order. The total gas emissivities $\varepsilon_{tot,gas}$ based on the LBL calculations and the WSGG model are compared in Fig. 8 demonstrating the accurate approximation.

3.6. GG models

The GG models applied within this study relied either on constant gas absorption coefficients K_{gas} that were a-priori obtained using the emissivity charts of Alberti et al. [53,54] and the mean beam length model (see Section 3.6.1) or on gas absorption coefficients K_{gas} that were calculated using the local total gas emissivities $\varepsilon_{gas,tot}$ predicted by the user-defined WSGG models (see Section 3.5) and the mean beam length model (see Section 3.6.1) or using the domain-based model (see Section 3.6.2).

[4] Accidentally, the expression (47) for the pressure path length in the preceding study [2] incorrectly included the gas species mole fraction of CO.

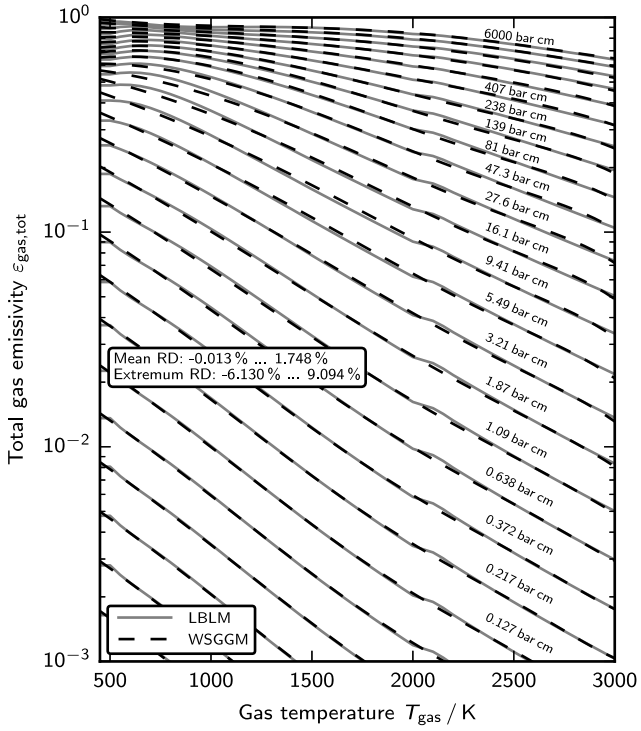

Fig. 8. Total gas emissivities calculated using the LBL model and the user-defined WSGG model for the bioliq EFG conditions.

3.6.1. Mean beam length model

The mean beam length model of Hottel and Sarofim [33] defines the (mean) gas absorption coefficient K_{gas} by [33]

$$K_{gas} = -\frac{\ln\left(1-\varepsilon_{gas,tot}\right)}{L_{mean}}, \tag{39}$$

where L_{mean} is the mean path length. The mean path length L_{mean} is defined by $3.6\,V/A_s$ for an arbitrary geometry with the volume V and the surface area A_s while it is given by $1.76\,L$ for a slab configuration with the length L.

3.6.2. Domain-based model

The domain-based model defined in ANSYS Fluent [30] relies on the WSGG model of Smith et al. [31], the scaling rules of Edwards and Matavosian [32], that provide tabulated coefficients for scaling the total gas emissivity $\varepsilon_{gas,tot}$ to total gas pressures p_{gas} of 0.1, 0.3, 3 and 10 atm at gas temperatures T_{gas} of 800, 1200, 1600 and 2000 K, and the mean beam length model (see Section 3.6.1).

3.6.3. User-defined GG model for REGA conditions

The user-defined gas absorption coefficient for the REGA conditions was previously [2] determined to be 0.53 m^{-1} using the total gas emissivity $\varepsilon_{gas,tot}$ for a typical gas condition in the REGA experiments and using the mean beam length model (see Section 3.6.1).

3.6.4. User-defined GG model for bioliq EFG conditions

The user-defined gas absorption coefficient for the bioliq EFG conditions was estimated to be 2.4 m^{-1} using the total gas emissivity $\varepsilon_{gas,tot}$ at the equilibrium gas condition and using the mean beam length model [33]. Thus, the gas absorption coefficient only slightly differs from the value that was used in the preceding studies [72,73] and was given by a value of 2.3 m^{-1} based on the exponential wide band model of Lallemant and Weber [74] and the mean beam length approach [33]. The reason is that even larger errors in the total gas emissivity and the actual gas species concentrations are not decisive due to the mean beam length model (see also Sections 4.2 and 4.4.4). Even the gas temperature has only a slight impact; for gas temperatures between 1350 K and 1850 K, gas absorption coefficients between 2.2 m^{-1} and 2.7 m^{-1} can be determined using the emissivity charts of Alberti et al. [53,54] and the mean beam length model [33].

3.7. SLWSGG models

The SLWSGG models were applied using (i) the reference gas condition approach, (ii) the absorption line blackbody distribution function (ALBDF) tables of Pearson et al. [34,35] and (iii) the multiplication method for mixtures. The reference gas condition approach relies on volumetric averaging of the gas pressure p_{gas}, the gas temperature T_{gas}, the gas species mole fraction of water vapour $x_{H_2O,gas}$, the gas species mole fraction of carbon dioxide $x_{CO_2,gas}$ and the gas species mole fraction of carbon monoxide $x_{CO,gas}$. For the slab configuration, the reference quantities were determined by [34]

$$X_{ref} = \frac{1}{2\,L}\sum_n \left(X_n + X_{n-1}\right)\left(z_n - z_{n-1}\right), \tag{40}$$

where $X = p_{gas}, T_{gas}, x_{H_2O,gas}, x_{CO_2,gas}, x_{CO,gas}$ and $\boldsymbol{z} = (z_n)$ are the node positions.

The absorption line blackbody distribution function (ALBDF) tables provide tabulated fractions of blackbody emission F for H_2O, CO_2 and CO below prescribed absorption cross-sections C and were generated using LBL calculations with the HITEMP-2010 databases [44], with the Voigt line-shape function and with cut-off criteria [34,35] (2750 half-widths for H_2O and 600 half-widths for CO_2 and CO). The ALBDF data has been given for 71 absorption cross-sections, for 28 gas temperatures T_{gas} between 300 K and 3000 K, for 28 blackbody temperatures T_b between 300 K and 3000 K, for 10 gas pressures p_{gas} between 0.1 bar and 50 bar and for 9 gas species mole fractions of water vapour $x_{H_2O,gas}$ and was accessed using linear interpolations following previous studies [34,35].

In addition to the reference (thermodynamic) gas state $\boldsymbol{\phi}_{gas,ref}$, reference supplemental absorption cross-sections $\boldsymbol{C}_{ref} = (C_{ref,k})$ were specified by [34,35]

$$C_{ref,k} = C_{min}\left(\frac{C_{max}}{C_{min}}\right)^{k/(21-1)} \tag{41}$$

where $C_{min} = 10^{-4}$ m^2/mol is the minimum absorption cross-section, $C_{max} = 10^3$ m^2/mol is the maximum cross-section and 21 is the number of recommended cross-sections (pseudo-bands).

The reference supplemental absorption cross-sections $\boldsymbol{C}_{ref} = (C_{ref,k})$ were applied to determine the reference ALBDF values $\boldsymbol{F}_{ref} = (F_{ref,k})$ defined by [34]

$$\begin{aligned} F_{ref,k} &= F_{mix}\left(C = C_{ref,k}, \boldsymbol{\phi} = \boldsymbol{\phi}_{gas,ref}, T_b = T_{gas,ref}\right) \\ &= \sum_{m=H_2O,CO_2,CO} F_m\left(C = C_{ref,k}/x_{m,gas,ref}, \boldsymbol{\phi} = \boldsymbol{\phi}_{gas,ref}, \right. \\ &\qquad \left. T_b = T_{gas,ref}\right), \end{aligned} \tag{42}$$

where $F_{mix}\left(C, \boldsymbol{\phi}, T_b\right)$ represents the ALBDF of the mixture based on the multiplication method, $F_m\left(C, \boldsymbol{\phi}, T_b\right)$ is the ALBDF of species m, $\boldsymbol{\phi}$ is the (thermodynamic) state, $\boldsymbol{\phi}_{gas,ref}$ is the (thermodynamic) reference gas state and T_b is the blackbody temperature.

Furthermore, local supplemental cross-sections $\boldsymbol{C} = (C_k)$ were determined by [34]

$$C_k = C\left(F = F_{ref,k}, \boldsymbol{\phi} = \boldsymbol{\phi}_{gas}, T_b = T_{gas,ref}\right), \tag{43}$$

where $C\left(F, \boldsymbol{\phi}, T_b\right)$ is the inverse ALBDF and $\boldsymbol{\phi}_{gas}$ is the (thermodynamic) gas state.

The weights $\boldsymbol{a}(T) = (a_k(T))$ and the gas absorption coefficients $\boldsymbol{K}_{gas} = (K_{gas,k})$ were finally (i. e. as incorporated into the radiative transfer equations) calculated by [34]

$$a_k(T) = \begin{cases} F\left(C = C_k, \boldsymbol{\phi} = \boldsymbol{\phi}_{\text{gas,ref}}, T_\text{b} = T\right), & \text{if } k = 0 \\ F\left(C = C_k, \boldsymbol{\phi} = \boldsymbol{\phi}_{\text{gas,ref}}, T_\text{b} = T\right) & \\ \quad - F\left(C = C_{k-1}, \boldsymbol{\phi} = \boldsymbol{\phi}_{\text{gas,ref}}, T_\text{b} = T\right), & \text{else} \end{cases}, \tag{44}$$

$$K_{\text{gas},k} = \begin{cases} 0, & \text{if } k = 0 \\ \dfrac{p_\text{gas}}{\overline{R}\, T_\text{gas}} \sqrt{C_k\, C_{k-1}}, & \text{else} \end{cases}. \tag{45}$$

3.8. FSCK models

The FSCK models were incorporated using the FSCK tables of Wang et al. [36] and the corresponding reference gas condition approach. The tables contain discrete full-spectrum correlated-k distributions for 34 total gas pressures p_gas between 0.1 bar and 80 bar, for 28 gas temperatures T_gas between 300 K and 3000 K, for 28 Planck temperatures T_P between 300 K and 3000 K, for 13 gas species mole fractions of water vapour $x_{\text{H}_2\text{O,gas}}$ between 0 and 1, for 13 gas species mole fractions of carbon dioxide $x_{\text{CO}_2\text{,gas}}$ between 0 and 1 and for 6 gas species mole fractions of carbon monoxide $x_{\text{CO,gas}}$ between 0 and 0.5 [36]. Each distribution was generated using LBL calculations with the HITEMP-2010 databases [44] and the Voigt line-shape function and was tabulated using 32 values corresponding to 32 quadrature nodes $\boldsymbol{g} = (g_k)$ and weights $\boldsymbol{w}_\text{FSCK} = (w_{\text{FSCK},k})$. The latter were defined using the nodes and weights of the Chebyshev polynomial of second kind and using subsequent transformation to improve the accuracy [75]. The transformation was carried out according to [75]

$$g_k := 1 - \left(1 - g_k\right)^\alpha, \tag{46}$$

$$w_{\text{FSCK},k} := \frac{\alpha\, w_{\text{FSCK},k}\, \left(1 - g_k\right)^{\alpha-1}}{\sum_i \alpha\, w_{\text{FSCK},i}\, \left(1 - g_i\right)^{\alpha-1}}, \tag{47}$$

where $\alpha = 2$ was previously found to be the most appropriate transformation factor [75].

The tables were accessed using linear interpolations following previous approach [36] except for the gas pressure p_gas. Corresponding to the operating pressures in the REGA and the bioliq EFG experiments, the tables for total gas pressures of 1 bar and 40 bar were applied only, i. e. interpolations were not performed with respect to the gas pressure.

The reference gas condition approach for the most recent FSCK tables relies on the Planck-averaged reference gas temperature $T_{\text{gas,P,ref}}$ only. For the 1D slab configuration, the Planck-averaged reference gas temperature $T_{\text{gas,P,ref}}$ was calculated by

$$T_{\text{gas,P,ref}} = \left(\frac{1}{2\,L}\, \frac{1}{K_{\text{P,ref}}} \sum_n \left(K_{\text{P},n}\, T_{\text{gas},n}^4 + K_{\text{P},n-1}\, T_{\text{gas},n-1}^4 \right) \left(z_n - z_{n-1}\right) \right)^{1/4}, \tag{48}$$

where

$$K_{\text{P},n} = \sum_k w_{\text{FSCK},k}\, a'_k\left(T_{\text{gas},n}\right)\, K'_k\left(T_{\text{gas},n}\right), \tag{49}$$

$$K_{\text{P,ref}} = \sum_k w_{\text{FSCK},k}\, a'_k\left(T_{\text{gas,P,ref}}\right)\, K'_k\left(T_{\text{gas,P,ref}}\right). \tag{50}$$

The weights $\boldsymbol{a}'(T) = \left(a'_k(T)\right)$ and the absorption coefficients $\boldsymbol{K}'(T) = \left(K'_k(T)\right)$ were determined by

$$a'_k(T) = a_\text{FSCK}\left(T = T, T_\text{P} = T, k = k\right), \tag{51}$$

$$K'_k(T) = K_\text{FSCK}\left(T = T, \boldsymbol{\phi} = \boldsymbol{\phi}_\text{gas}, T_\text{P} = T, g = g_k\right), \tag{52}$$

where a_FSCK and K_FSCK are functions for calculating the weights and the absorption coefficients with respect to the FSCK tables. The former is defined by

$$a_\text{FSCK}\left(T, T_\text{P}, k\right) = \begin{cases} \dfrac{1}{g'_k}\, g_\text{FSCK}\left(T, K'_k\left(T, T_\text{P}\right)\right), & \text{if } k = 0 \\ \dfrac{1}{g'_k - g'_{k-1}} \left(g_\text{FSCK}\left(T, K'_k\left(T, T_\text{P}\right)\right) \right. & \\ \quad \left. - g_\text{FSCK}\left(T, K'_{k-1}\left(T, T_\text{P}\right)\right)\right), & \text{else} \end{cases}, \tag{53}$$

where

$$g_\text{FSCK}\left(T, K'_k\left(T, T_\text{P}\right)\right) = g_\text{FSCK}\left(T = T, \boldsymbol{\phi} = \boldsymbol{\phi}_\text{gas}, T_\text{P} = T, K = K'_k\left(T, T_\text{P}\right)\right), \tag{54}$$

$$K'_k\left(T, T_\text{P}\right) = K_\text{FSCK}\left(T = T, \boldsymbol{\phi} = \boldsymbol{\phi}_\text{gas}, T_\text{P} = T_\text{P}, g = g'_k\right), \tag{55}$$

$$g'_k = \sum_i^k w_{\text{FSCK},i}. \tag{56}$$

Here, g_FSCK is the inverse function for calculating the fraction of the spectrum below the specified absorption coefficient.

The weights $\boldsymbol{a}(T) = \left(a_k(T)\right)$ and the gas absorption coefficients $\boldsymbol{K}_\text{gas} = \left(K_{\text{gas},k}\right)$ were finally (i. e. as incorporated into the radiative transfer equations) determined by

$$a_k(T) = a_\text{FSCK}\left(T = T, T_\text{P} = T_{\text{gas,P,ref}}, k = k\right), \tag{57}$$

$$K_{\text{gas},k} = K_\text{FSCK}\left(T = T_\text{gas}, \boldsymbol{\phi} = \boldsymbol{\phi}_\text{gas}, T_\text{P} = T_{\text{gas,P,ref}}, g = g_k\right). \tag{58}$$

3.9. Soot contributions

Soot contributions for bioliq EFG conditions were approximated by the correlation of Felske and Tien [76]. The mean soot absorption coefficient K_soot was accordingly described by [76]

$$K_\text{soot} = 3.72\, f_\text{v,soot}\, C_\text{soot}\, \frac{T}{C_2}, \tag{59}$$

where $f_\text{v,soot}$ is the soot volume fraction, C_soot is the soot constant, T is the temperature and C_2 is $1.4387... \cdot 10^{-2}$ m K. The soot volume fraction $f_\text{v,soot}$ is correlated with the soot mass fraction w_soot by

$$f_\text{v,soot} = w_\text{soot}\, \frac{\rho_\text{gas}}{\rho_\text{soot}}, \tag{60}$$

where ρ_gas is the gas density and ρ_soot is the soot density (typically between 1600 kg/m^3 and 2000 kg/m^3).

Soot volume fraction $f_\text{v,soot}$ and soot constant C_soot were regarded as model parameters within the sensitivity analysis (see Section 4.4.5) as soot measurements in the bioliq EFG have not been performed yet. Generally, soot concentrations are expected to be rather low for the gasification of ethylene glycol since (i) far-flame soot measurements in REGA experiments demonstrated soot concentrations below the detection limit [77] and (ii) observations from bioliq EFG experiments have indicated quite low soot concentrations. However, larger soot contents are rather likely for the gasification of pyrolysis oils and slurries. For a few bioliq EFG experiments with pyrolysis oils at atypical, low-temperature process conditions, soot mass fractions w_soot up to 1–3% were determined from balancing (neglecting further by-products as hydrocarbons). This corresponds to soot volume fractions $f_\text{v,soot}$ of approximately 10^{-5}-10^{-4}. For REGA experiments with glycol slurries containing 10% pyrolysis char [77], soot volume fractions of 10^{-8} were estimated from measurements. These findings are in agreement with measurements and predictions reported elsewhere [21,78–81]. For example, Sepman et al. [78] and Simonsson et al. [79] measured soot volume fractions in the order of 10^{-6} in atmospheric entrained flow gasification experiments with wood and peat powders. For gasification of heavy oil, Bader et al. [81] predicted soot mass fractions of approximately 2% using CFD simulations.

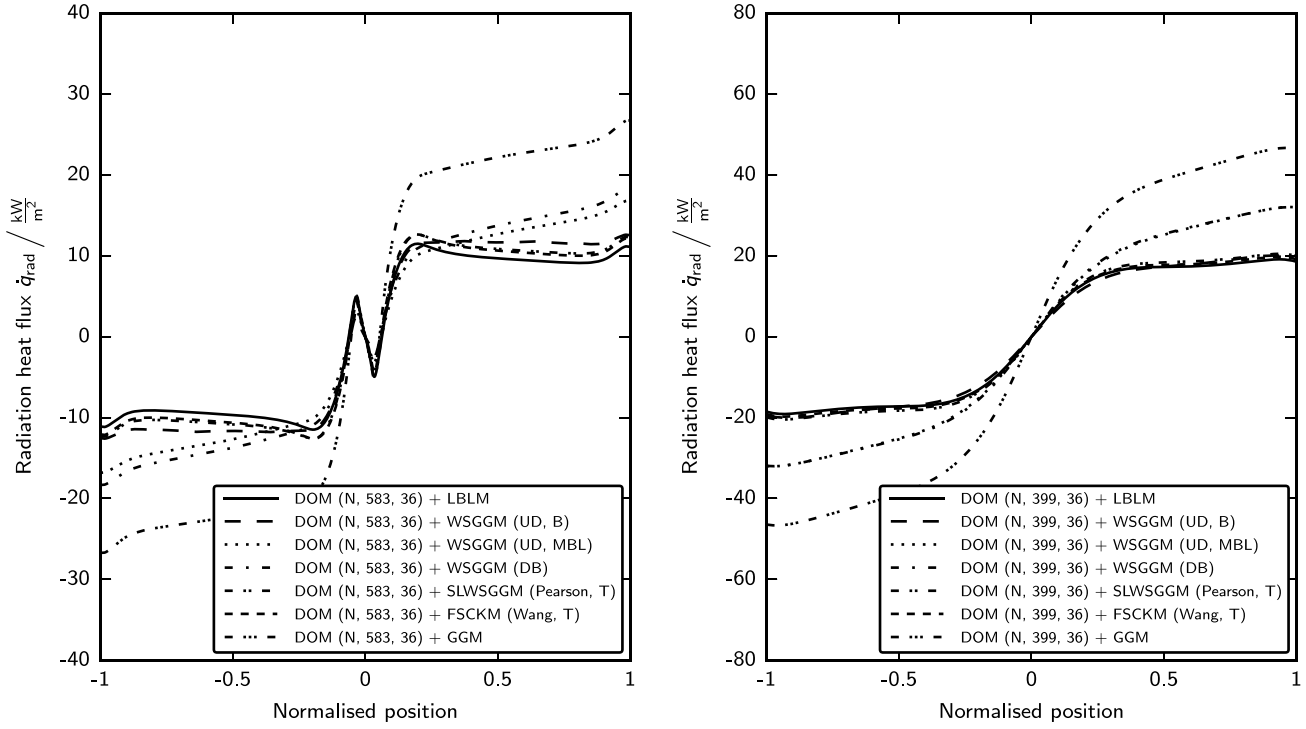

Fig. 9. Predicted heat flux profiles for the REGA experiment TUC3 V786 at the nozzle distances of 100 mm (left) and 300 mm (right) based on 1D slab simulations.

4. Results

This section presents the results of the 1D slab simulations at atmospheric and high-pressure entrained flow gasification conditions, discusses the results of the sensitivity analyses with the 1D slab configuration and with emphasis on high-pressure conditions and finally reports on the results of the CFD simulations of the bioliq EFG experiment.

4.1. 1D slab simulations for REGA conditions

Simplified gas radiation property models were previously suggested for the CFD model of the REGA due to computing time reasons [2,7]. Relying either on the user-defined WSGG model for REGA conditions or on the user-defined GG model for the REGA conditions, similar predictions of gas species concentrations and total wall heat fluxes were obtained in the CFD simulations of the REGA experiments while larger deviations were found in gas temperatures and in radiation wall heat fluxes [2,7]. As CFD simulations cannot currently be performed using absorption spectra, 1D slab simulations based on the DO model and different gas radiation property models were carried out to investigate the preceding approach.

The results are compared in Figs. 9 and 10. Radiation heat fluxes based on the user-defined WSGG model combined with the band approach, based on the ALBDF tables and based on the FSCK tables are accordingly in good agreement with the predictions based on the LBL model. Heat sources are thus predicted accurately as demonstrated using the absolute relative deviations (ARD) in Tables 1–4. Significant deviations are found with respect to the user-defined GG model for the REGA conditions. However, this very poor performance can be explained by the mean beam length approach. As the mean beam length of the REGA is smaller than the mean beam length of the slab configuration, the grey-gas absorption coefficient is overestimated for this configuration. More meaningful grey-gas predictions are thus provided by the user-defined WSGG model combined with the mean beam length of the slab configuration but are still poorer than the predictions based on the user-defined WSGG model combined with the band approach.

Table 1
Predicted absolute radiation wall heat fluxes $|\dot{q}_{rad,wall}|$ and absolute relative deviations (ARD) with respect to the radiation wall heat fluxes, radiation heat source terms and incident radiations for the REGA experiment TUC3 V786 at the nozzle distance of 100 mm based on 1D slab simulations with the DO model and with various gas radiation property models.

Gas radiation property model	$\frac{\lvert\dot{q}_{rad,wall}\rvert}{kW/m^2}$	$\frac{ARD_q}{\%}$	$\frac{ARD_S}{\%}$	$\frac{ARD_G}{\%}$
LBLM	11.11			
WSGGM (UD, B)	13.09	17.79	32.10	0.39
WSGGM (UD, MBL)	17.55	57.94	52.59	1.47
WSGGM (DB)	18.34	65.12	52.39	1.65
SLWSGGM (Pearson, T)	12.34	11.04	7.76	0.33
SLWSGGM (Pearson, T-6)	14.75	32.74	57.21	0.94
SLWSGGM (Pearson, T-32)	12.29	10.60	6.37	0.32
FSCKM (Wang, T)	12.08	8.76	6.45	0.28
GGM (UD)	26.73	140.62	63.50	3.77

This finally justifies the implementation of the latter approach for the CFD model of the REGA. Only if this approach already exceeds the available computing resources for optically thin conditions prevailing in atmospheric entrained flow gasification, user-defined GG models may be applied. However, this may increase the inaccuracies in the predictions of gas and wall temperatures and radiation wall heat fluxes (see [2,7]) through erroneous radiation heat source terms.

4.2. 1D slab simulations for bioliq EFG conditions

Simplified gas radiation property models for the CFD model of the bioliq EFG relied first [72,73] on a GG model and later [6] on the user-defined WSGG model for bioliq EFG conditions in combination with the band approach. Since preliminary CFD simulations indicated significantly deviating total heat flux predictions, 1D slab simulations based on the DO model and different gas radiation property models were used to investigate the best approach for the CFD simulations.

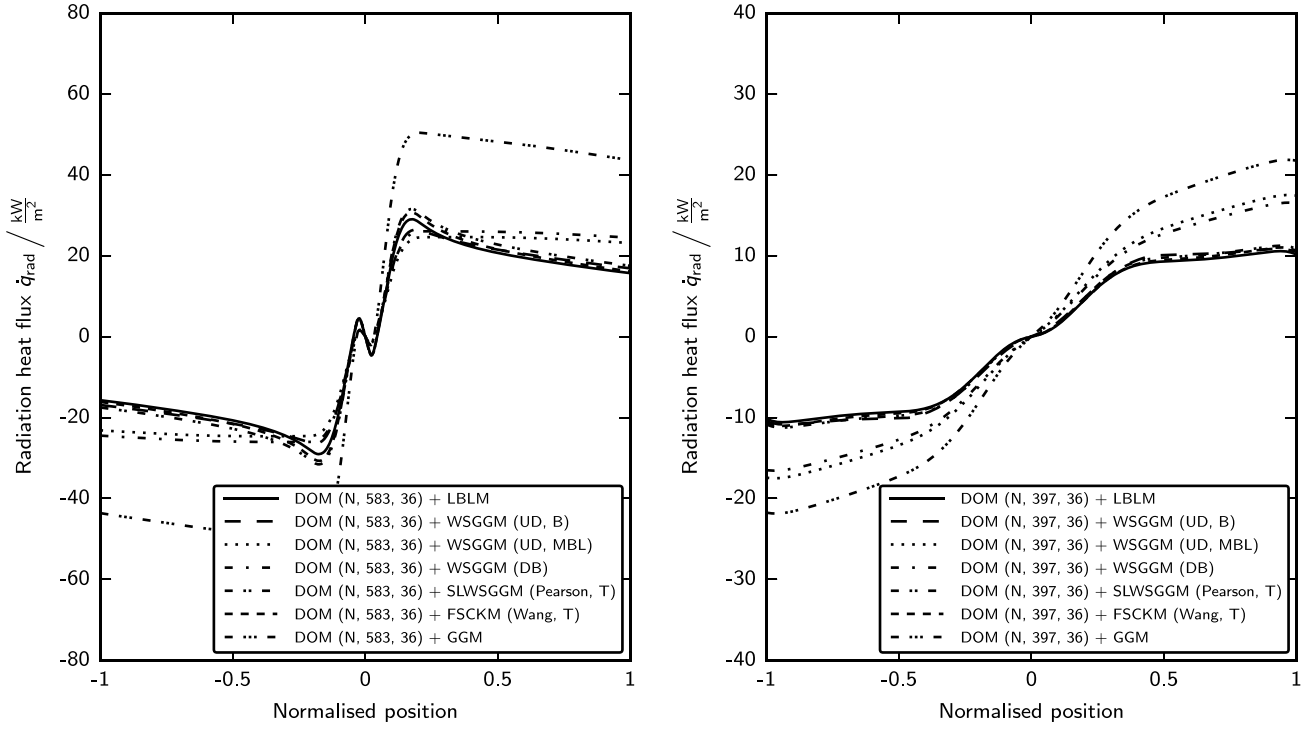

Fig. 10. Predicted heat flux profiles for the REGA experiment TUC5 V1105 at the nozzle distances of 100 mm (left) and 300 mm (right) based on 1D slab simulations.

Table 2
Predicted absolute radiation wall heat fluxes $|\dot{q}_{rad,wall}|$ and absolute relative deviations (ARD) with respect to the radiation wall heat fluxes, radiation heat source terms and incident radiations for the REGA experiment TUC3 V786 at the nozzle distance of 300 mm based on 1D slab simulations with the DO model and with various gas radiation property models.

Gas radiation property model	$\frac{\lvert\dot{q}_{rad,wall}\rvert}{kW/m^2}$	$\frac{ARD_q}{\%}$	$\frac{ARD_S}{\%}$	$\frac{ARD_G}{\%}$
LBLM	18.54			
WSGGM (UD, B)	19.98	7.75	15.37	0.17
WSGGM (UD, MBL)	33.05	78.22	73.24	3.29
WSGGM (DB)	31.96	72.32	67.71	3.05
SLWSGGM (Pearson, T)	20.02	7.98	7.49	0.37
SLWSGGM (Pearson, T-6)	23.62	27.39	27.42	1.21
SLWSGGM (Pearson, T-32)	19.95	7.56	7.09	0.35
FSCKM (Wang, T)	19.14	3.22	4.48	0.15
GGM (UD)	46.46	150.52	141.14	6.20

Table 3
Predicted absolute radiation wall heat fluxes $|\dot{q}_{rad,wall}|$ and absolute relative deviations (ARD) with respect to the radiation wall heat fluxes, radiation heat source terms and incident radiations for the REGA experiment TUC5 V1105 at the nozzle distance of 100 mm based on 1D slab simulations with the DO model and with various gas radiation property models.

Gas radiation property model	$\frac{\lvert\dot{q}_{rad,wall}\rvert}{kW/m^2}$	$\frac{ARD_q}{\%}$	$\frac{ARD_S}{\%}$	$\frac{ARD_G}{\%}$
LBLM	15.72			
WSGGM (UD, B)	17.30	10.08	24.02	0.41
WSGGM (UD, MBL)	23.85	51.78	46.67	1.84
WSGGM (DB)	24.47	55.68	45.47	2.04
SLWSGGM (Pearson, T)	17.58	11.85	8.26	0.76
SLWSGGM (Pearson, T-6)	21.36	35.94	48.55	2.21
SLWSGGM (Pearson, T-32)	17.52	11.46	7.48	0.73
FSCKM (Wang, T)	16.13	2.62	6.35	0.31
GGM (UD)	43.63	177.64	55.52	8.43

The results are shown in Fig. 11. Accordingly, the user-defined WSGG model combined with the band approach, the SLWSGG model and the FSCK model provide predictions that are in good agreement with the predictions based on the LBL model. Large deviations are obvious for the predictions using the user-defined GG model and those WSGG models that are combined with the mean beam length approach (see Section 4.1). However, the radiation wall heat fluxes at 260 mm and 1524 mm are predicted quite well by all simplified models with exception of the user-defined GG model and the user-defined WSGG model combined with the mean beam length approach as shown in Tables 5 and 6. More specifically, the domain-based model is accurate realising that it was developed for atmospheric combustion conditions based on emissivity models that are nowadays regarded as inaccurate. The good performance of the domain-based model can be explained by the mean beam length approach. Even larger errors in the prediction of the total gas emissivity do not affect the mean gas absorption coefficient significantly. Therefore, the correct magnitude of the

Table 4
Predicted absolute radiation wall heat fluxes $|\dot{q}_{rad,wall}|$ and absolute relative deviations (ARD) with respect to the radiation wall heat fluxes, radiation heat source terms and incident radiations for the REGA experiment TUC5 V1105 at the nozzle distance of 300 mm based on 1D slab simulations with the DO model and with various gas radiation property models.

Gas radiation property model	$\frac{\lvert\dot{q}_{rad,wall}\rvert}{kW/m^2}$	$\frac{ARD_q}{\%}$	$\frac{ARD_S}{\%}$	$\frac{ARD_G}{\%}$
LBLM	10.18			
WSGGM (UD, B)	10.83	6.63	9.94	0.07
WSGGM (UD, MBL)	17.89	75.71	70.87	2.19
WSGGM (DB)	16.51	62.20	58.29	1.80
SLWSGGM (Pearson, T)	10.91	7.16	6.66	0.23
SLWSGGM (Pearson, T-6)	12.57	23.44	24.44	0.72
SLWSGGM (Pearson, T-32)	10.87	6.80	6.34	0.22
FSCKM (Wang, T)	10.63	4.38	5.91	0.12
GGM (UD)	21.76	113.74	106.19	3.24

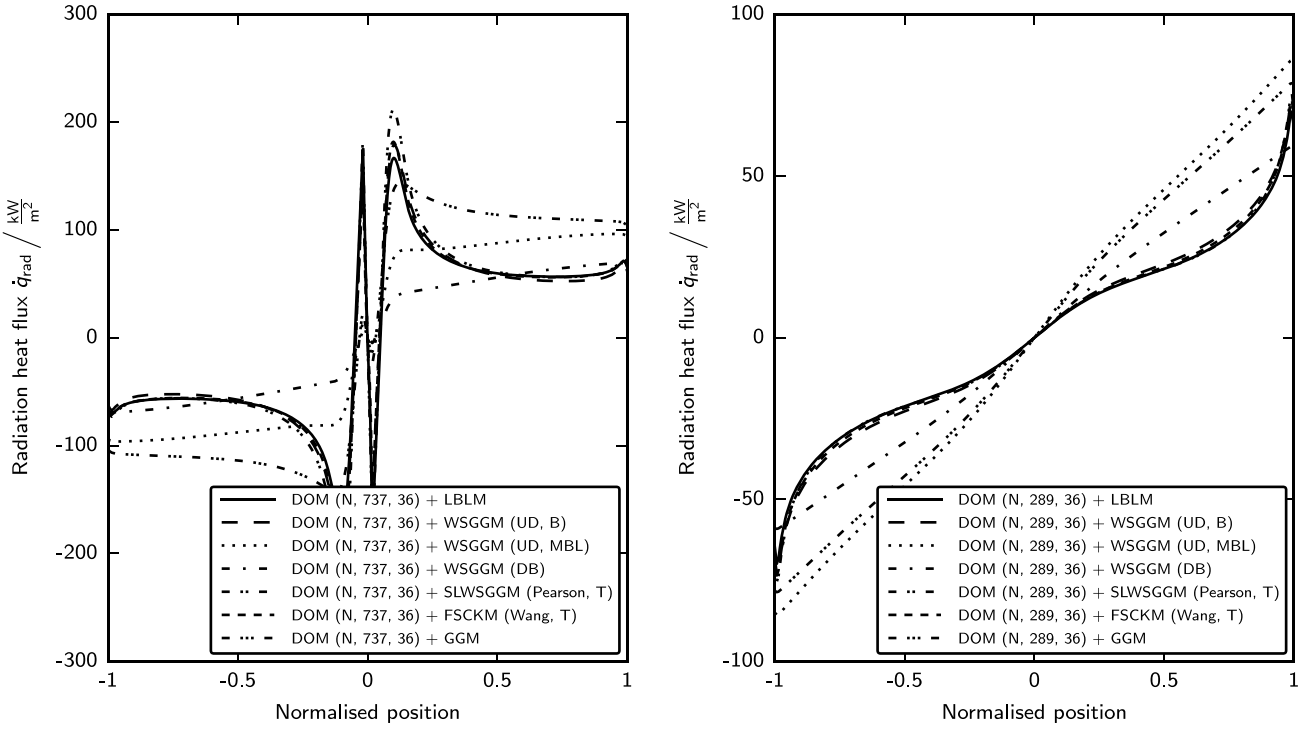

Fig. 11. Predicted heat flux profiles for the bioliq EFG experiment V82.1 at the nozzle distances of 260 mm (left) and 1524 mm (right) based on 1D slab simulations.

Table 5
Predicted absolute radiation wall heat fluxes $|\dot{q}_{rad,wall}|$ and absolute relative deviations (ARD) with respect to the radiation wall heat fluxes, radiation heat source terms and incident radiations for the bioliq EFG experiment V82.1 at the nozzle distance of 260 mm based on 1D slab simulations with the DO model and with various gas radiation property models.

Gas radiation property model	$\frac{\lvert\dot{q}_{rad,wall}\rvert}{kW/m^2}$	$\frac{ARD_q}{\%}$	$\frac{ARD_S}{\%}$	$\frac{ARD_G}{\%}$
LBLM	65.79			
WSGGM (UD, B)	61.72	6.19	12.89	1.69
WSGGM (UD, MBL)	94.25	43.25	87.37	16.55
WSGGM (DB)	68.70	4.41	96.84	29.85
SLWSGGM (Pearson, T)	66.89	1.67	18.18	7.21
SLWSGGM (Pearson, T-6)	65.82	0.04	22.89	5.70
SLWSGGM (Pearson, T-32)	67.12	2.02	18.74	7.27
FSCKM (Wang, T)	65.55	0.38	9.42	3.11
GGM (UD)	104.17	58.33	68.29	9.97

Table 6
Predicted absolute radiation wall heat fluxes $|\dot{q}_{rad,wall}|$ and absolute relative deviations (ARD) with respect to the radiation wall heat fluxes, radiation heat source terms and incident radiations for the bioliq EFG experiment V82.1 at the nozzle distance of 1524 mm based on 1D slab simulations with the DO model and with various gas radiation property models.

Gas radiation property model	$\frac{\lvert\dot{q}_{rad,wall}\rvert}{kW/m^2}$	$\frac{ARD_q}{\%}$	$\frac{ARD_S}{\%}$	$\frac{ARD_G}{\%}$
LBLM	64.83			
WSGGM (UD, B)	68.34	5.41	6.23	0.15
WSGGM (UD, MBL)	85.01	31.11	78.01	1.92
WSGGM (DB)	58.93	9.10	60.75	8.84
SLWSGGM (Pearson, T)	69.72	7.55	9.34	2.08
SLWSGGM (Pearson, T-6)	68.77	6.07	13.09	1.80
SLWSGGM (Pearson, T-32)	69.83	7.71	9.57	2.13
FSCKM (Wang, T)	68.20	5.19	5.09	1.23
GGM (UD)	78.23	20.67	74.30	3.89

total gas emissivity is sufficient, which is granted by the domain-based model for bioliq EFG conditions. Recalling that the mean beam length approach was defined to provide good predictions of the radiation wall heat fluxes only, this deficiency can clearly be seen in the predictions relying on the mean beam length approach in Fig. 11.

4.3. Computing times

Computing times of 1D slab simulations, although significantly lower than those of coupled 2D or 3D radiation simulations, can illustrate the computational expense for different gas radiation property models. Therefore, mean computing times of the 1D slab simulations, described in Sections 4.1 and 4.2, were determined by neglecting, as far as possible, one-time operations (for example, loading of tabulated values) and by averaging the computing times of up to 20 single simulations. Realising that the gas radiation property models rely on different numbers of pseudo-bands, mean computing times were also obtained for 1D slab simulations based on the DO model and the SLWSGG model with 6 or 32 cross-sections instead of the default 21 cross-sections to enable a comparison with the user-defined WSGG model combined with the band approach (6 pseudo-bands) and the FSCK model (32 pseudo-bands). The mean values are summarised in Table 7 and indicate the following ranking: GG model < WSGG model combined with the mean beam length approach < WSGG model combined with the band approach < FSCK model < SLWSGG model < LBL model. Although the relative standard deviations for the computing times of the 1D slab simulations using GG or WSGG models were quite high (up to 40%), this ranking is in accordance with the expectations except for the SLWSGG model. The computing times for 1D slab simulations using the SLWSGG model even with 6 cross-sections were higher than for simulations using the FSCK model due to the expensive calculation of local supplemental cross-sections based on the inverse ALBDF. Thus, the adopted methods [34] should be improved in future studies. In this context, it should also be noted that the application of 6 cross-sections significantly increases the absolute relative deviations for atmospheric conditions whereas increasing the number of cross-section to 32 changes the predictions only slightly (see Tables 1–6).

Table 7
Mean computing times of the 1D slab simulations with the DO model and with various gas radiation property models for the REGA experiments TUC3 V786 and TUC5 V1105 and for the bioliq EFG experiment V82.1.

Gas radiation property model	Number of pseudo-bands	Computing time/s					
		REGA TUC3 V786		REGA TUC5 V1105		bioliq EFG V82.1	
		100 mm	300 mm	100 mm	300 mm	260 mm	1524 mm
LBLM	$3 \cdot 10^6$	$4.5 \cdot 10^4$	$2.9 \cdot 10^4$	$4.5 \cdot 10^4$	$3.0 \cdot 10^4$	$4.2 \cdot 10^4$	$1.8 \cdot 10^4$
WSGGM (UD, B)	6	0.091	0.059	0.079	0.056	0.110	0.049
WSGGM (UD, MBL)	1	0.019	0.013	0.022	0.014	0.039	0.016
WSGGM (DB)	1	0.018	0.016	0.020	0.012	0.031	0.015
SLWSGGM (Pearson, T)	21	2.400	1.718	2.451	1.621	2.702	0.971
SLWSGGM (Pearson, T-6)	6	0.659	0.464	0.643	0.467	0.744	0.271
SLWSGGM (Pearson, T-32)	32	3.770	2.677	3.779	2.521	4.195	1.500
FSCKM (Wang, T)	32	0.413	0.289	0.414	0.293	0.267	0.122
GGM (UD)	1	0.015	0.010	0.017	0.011	0.017	0.009

Therefore, based on the comparisons of radiation wall heat fluxes, absolute relative deviations and computing times, only customised WSGG models combined with the band approach and the latest FSCK tables [36] can be recommended for radiation simulations at ambient and high-pressure entrained flow gasification conditions. The FSCK models with 32 pseudo-bands provide more accurate predictions while customised WSGG models with 4–7 pseudo-bands require significantly less computing resources and are thus a good compromise between computing time and accuracy. However, in absence of such customised models, the latest FSCK tables (or even FSCK tables with less pseudo-bands which have yet to be compiled) may be incorporated into CFD models of entrained flow gasification processes.

4.4. Sensitivity analyses

Optically thick conditions can be expected for high-pressure entrained flow gasification due to large partial pressures of H_2O, CO_2 and CO and can be demonstrated using estimates for the absorption coefficients in the bioliq EFG experiment V82.1. Applying the predictions of the 1D slab simulations based on the DO model and the LBL model, Rosseland-mean absorption coefficients K_R were determined using the semi-grey P-1 approximation

$$K_R = -\frac{1}{3}\frac{1}{\dot{q}_{rad}}\frac{dG}{dz}. \tag{61}$$

Mean non-uniform absorption coefficients K_{fit} were additionally estimated using the *least_squares* method of SciPy [82,83] and 1D slab simulations based on the DO model and the GG model, i. e. the radiation heat flux predictions based on the DO model and the GG model were fitted to the radiation heat fluxes that were obtained from the 1D slab simulation based on the DO model and the LBL model.

Following the discussion in the preceding study [2], mean absorption coefficients were also obtained by

$$K_{WSSG} = \sum_k a_k K_{p,gas,k} \left(x_{H_2O,gas} + x_{CO_2,gas}\right) \tag{62}$$

with the weights $\boldsymbol{a} = (a_k)$ and the pressure-based gas absorption coefficients $\boldsymbol{K}_{p,gas} = (K_{p,gas,k})$ of the user-defined WSGG model.

The Rosseland-mean absorption coefficients K_R and the fitted-mean absorption coefficients K_{fit} are depicted alongside the WSGG-mean absorption coefficients K_{WSGG} in Fig. 12. Despite the uncertainties due to the underlying model assumptions, the estimates for the absorption coefficients demonstrate that high mean absorption coefficients prevail in the boundary layer and that the values are larger in the boundary layer than in the bulk. Thus, thermal radiation in the boundary layer of the bioliq EFG primarily determines the radiation heat removal and has to be described well in the CFD model.

In order to identify uncertainties in the radiation predictions using the CFD model, non-coupled sensitivity analyses using the 1D slab model were performed with respect to model approaches, gas conditions and soot. The impacts of the boundary layer discretisation and of the radiation model are discussed in Sections 4.4.1 and 4.4.2. The influences of gas temperature, of gas species concentrations and of soot are presented in Sections 4.4.3, 4.4.4 and 4.4.5.

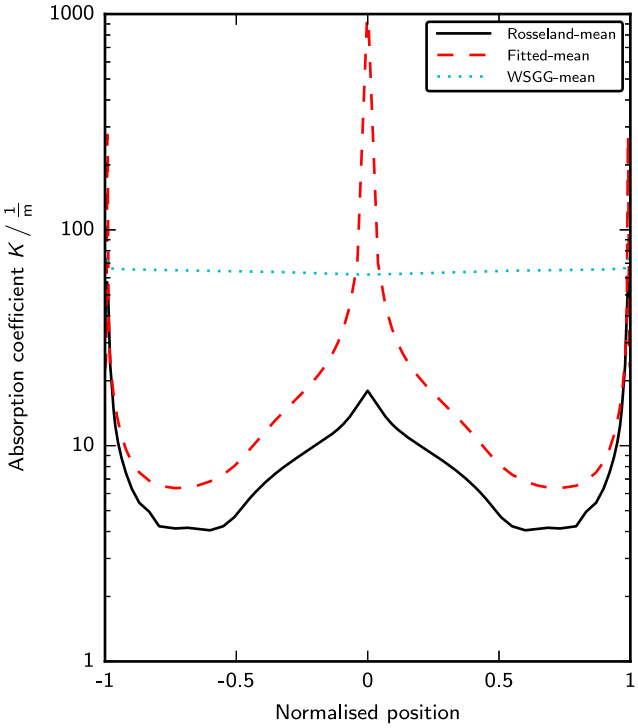

Fig. 12. Predicted absorption coefficient profiles for the bioliq EFG experiment V82.1 at the nozzle distance of 1524 mm.

4.4.1. Discretisation

Wall functions were applied in the CFD model of the bioliq EFG for computing time reasons. Since temperature gradients were accordingly only coarsely resolved, additional 1D slab simulations based on the DO model and the LBL model and based on the DO model and the user-defined WSGG model (combined with the band approach) were performed to investigate the influence of the boundary layer discretisation on the prediction of the heat removal.

The extracted and mirrored gas temperature and gas species mole fractions profiles at 1524 mm with 289 nodes (CFD mesh) were interpolated on two new meshes that were obtained using the gas temperature gradient and are characterised by 159 nodes (medium mesh) and 319 nodes (fine mesh) and resolve the boundary layer. The interpolated gas temperature profiles are depicted in Fig. 13 demonstrating the different non-equidistant node distributions. Thus, for computing time reasons, this is not a typical mesh independence analysis applying meshes with different equidistant node distributions. Rather, predictions based on different meshes with a fine resolution (319 nodes), a medium resolution (159 nodes) and a coarse resolution (289 nodes)

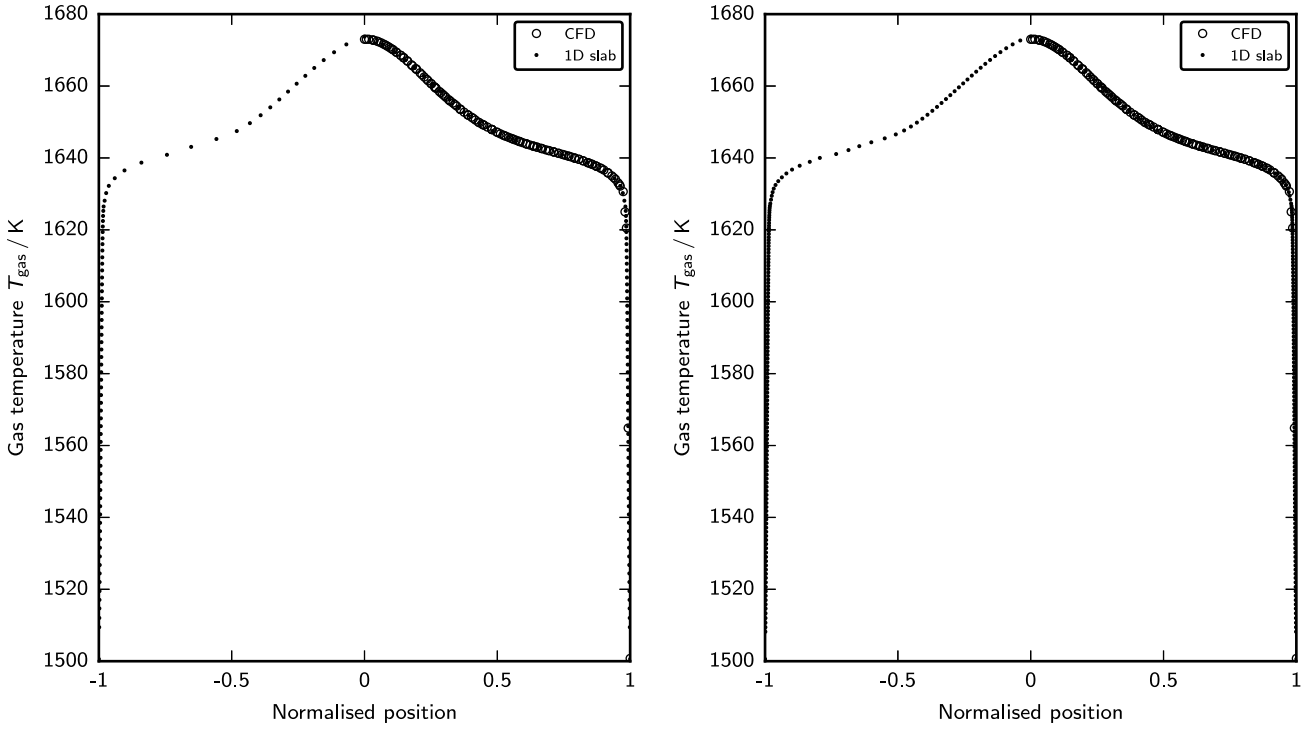

Fig. 13. Interpolation based gas temperature profiles for the bioliq EFG experiment V82.1 at the nozzle distance of 1524 mm using meshes with 159 nodes (left) and 319 nodes (right).

Table 8
Predicted absolute radiation wall heat fluxes $|\dot{q}_{rad,wall}|$ and absolute relative deviations (ARD) with respect to the radiation wall heat fluxes for the bioliq EFG experiment V82.1 at the nozzle distance of 1524 mm based on 1D slab simulations with the DO model or the P-1 model, with the LBL model or the user-defined WSGG model (combined with the band approach) and with various meshes. The predictions based on the DO model and the respective gas absorption coefficient model for the mesh with 319 nodes were defined as baseline results.

Model	Mesh	$\frac{\lvert\dot{q}_{rad,wall}\rvert}{kW/m^2}$		$\frac{ARD_q}{\%}$	
		LBLM	WSGGM	LBLM	WSGGM
DOM	Fine (319 nodes, baseline)	66.50	69.97		
	Medium (159 nodes)	66.31	69.76	0.30	0.30
	Coarse/CFD (289 nodes)	64.83	68.34	2.52	2.22
P1M	Fine (319 nodes)	71.80	75.99	7.96	8.60
	Medium (159 nodes)	71.90	76.10	8.12	8.77
	Coarse/CFD (289 nodes)	71.51	75.57	7.53	8.00

of the boundary layer are compared to analyse the effects on the heat removal.

The predicted radiation heat flux profiles are compared in Fig. 14. Only small deviations can be found near the walls. This is also evident from the radiation wall heat fluxes given in Table 8. In comparison with the baseline prediction using the fine mesh with 319 nodes, the radiation wall heat fluxes predicted using the medium mesh deviate only 0.3% while the radiation wall heat fluxes predicted using the CFD mesh differ up to 2.5%. Thus, the fine mesh is able to provide meaningful reference results, and the CFD mesh can be accepted for coupled radiation simulations.

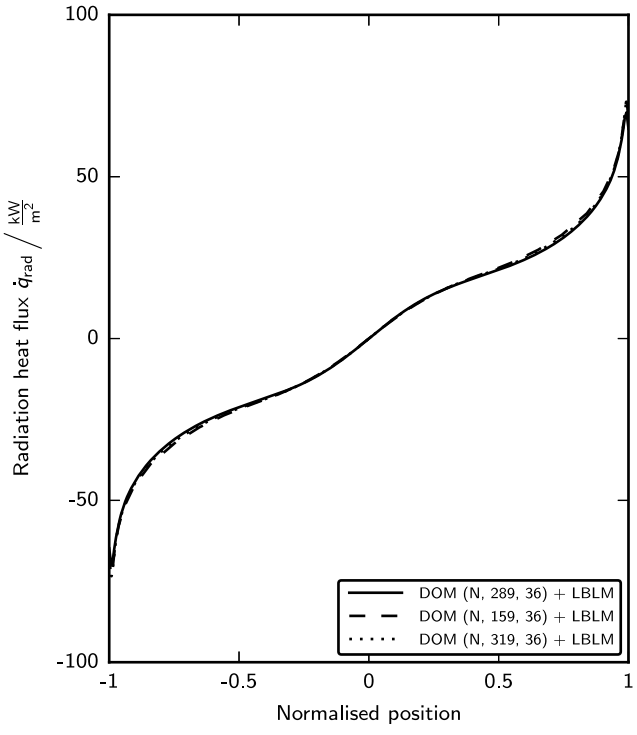

Fig. 14. Predicted radiation heat flux profiles for the bioliq EFG experiment V82.1 at the nozzle distance of 1524 mm based on 1D slab simulations using various meshes.

4.4.2. P-1 approximation

CFD simulations of the bioliq EFG were carried out using the DO model. However, the optically thick gas conditions enable to apply the P-1 model to reduce the computing times. Therefore, additional uncoupled 1D slab simulations based on the P-1 model and the LBL model

Table 9
Predicted absolute radiation wall heat fluxes $|\dot{q}_{rad,wall}|$ and absolute relative deviations (ARD) with respect to the radiation wall heat fluxes for the bioliq EFG experiment V82.1 at the nozzle distance of 1524 mm based on 1D slab simulations with the DO model and the LBL model and with various gas temperature profiles. The predictions based on the DO model and the LBL model for the mesh with 319 nodes were defined as baseline results.

Case	$\frac{\lvert\dot{q}_{rad,wall}\rvert}{kW/m^2}$	$\frac{ARD_q}{\%}$
Baseline	66.50	
T +	80.43	20.94
T −	54.18	18.52

and based on the P-1 model and the user-defined WSGG model (combined with the band approach) were performed to investigate the influence of the radiation model. The predicted radiation wall heat fluxes for the different meshes are given in Table 8. If the results based on the DO model, the respective gas absorption coefficient model and the mesh with 319 nodes are regarded as the most accurate predictions, the results in Table 8 demonstrate that the loss of accuracy is around 8% and is quite similar for the different meshes when the P-1 approximation is used instead of the DO model. Thus, small deviations can also be expected for coupled radiation simulations using the CFD discretisation. Interestingly, deviations for the CFD mesh are more accurate than predictions based on the medium and the fine mesh. However, these small deviations should not be over-interpreted as the meshes are characterised by non-equidistant node distributions.

4.4.3. Gas temperature

Simplified description of slag deposition and slag flow in the CFD model of the bioliq EFG leads to uncertainties in the gas temperature predictions. Since the impact of gas temperature on radiation predictions is well known, 1D slab simulations based on the DO model and the LBL model and based on the DO model and the user-defined WSGG model (combined with the band approach) were carried out with various gas temperature profiles for numerical comparison only. The gas temperatures were separately increased by 5% (+) or decreased by 5% (−). The predicted radiation wall heat fluxes are summarised in Table 9 showing the strong impact of the gas temperature. However, it needs to be noted again that the simulations were uncoupled, i. e. the gas temperature remained constant while using the DO model.

4.4.4. Gas composition

Simplified gas chemistry was applied in the CFD model of the bioliq EFG in view of the fact that a reaction mechanism for the gasification of ethylene glycol has not been validated yet for high-pressure conditions. Since uncertainties of global reaction mechanisms in the water-gas-shift reaction rates and in the consumption rates of methane impede accurate predictions of gas species concentrations (see [84]), 1D slab simulations based on the DO model and the LBL model were performed to study the radiation heat flux predictions with various gas species mole fractions profiles of H_2O, CO_2 and CO. The gas species mole fractions were separately increased (+) or decreased (−), each by 5%.

The predicted radiation wall heat fluxes are compared in Tables 10 and 11 demonstrating very small relative deviations from the baseline predictions. Inaccurate predictions of gas species concentrations, within the ± 5% margin, are thus not significant for the radiation simulations.

4.4.5. Soot

Soot was neglected in the CFD model of the bioliq EFG as bioliq EFG experiments with ethylene glycol at higher operating temperatures have indicated low soot concentrations (see Section 3.9). In order to determine at what soot volume fraction $f_{v,soot}$ the currently predicted radiation heat fluxes would be substantially altered, 1D slab simulations using the DO model and the LBL model were performed

Table 10
Predicted absolute radiation wall heat fluxes $|\dot{q}_{rad,wall}|$ and absolute relative deviations (ARD) with respect to the radiation wall heat fluxes for the bioliq EFG experiment V82.1 at the nozzle distance of 260 mm based on 1D slab simulations with the DO model and the LBL model and with various gas species mole fractions profiles. The predictions based on the DO model and the LBL model for the mesh with 319 nodes were defined as baseline results.

Case	$\frac{\lvert\dot{q}_{rad,wall}\rvert}{kW/m^2}$	$\frac{ARD_q}{\%}$
Baseline	65.79	
H_2O +	65.85	0.09
H_2O −	65.72	0.11
CO_2 +	65.76	0.04
CO_2 −	65.83	0.05
CO +	65.83	0.05
CO −	65.76	0.05

Table 11
Predicted absolute radiation wall heat fluxes $|\dot{q}_{rad,wall}|$ and absolute relative deviations (ARD) with respect to the radiation wall heat fluxes for the bioliq EFG experiment V82.1 at the nozzle distance of 1524 mm based on 1D slab simulations with the DO model and the LBL model and with various gas species mole fractions profiles. The predictions based on the DO model and the LBL model for the mesh with 319 nodes were defined as baseline results.

Case	$\frac{\lvert\dot{q}_{rad,wall}\rvert}{kW/m^2}$	$\frac{ARD_q}{\%}$
Baseline	66.50	
H_2O +	66.52	0.03
H_2O −	66.31	0.29
CO_2 +	66.68	0.27
CO_2 −	66.52	0.02
CO +	66.49	0.03
CO −	66.49	0.02

alongside 1D slab simulations using the DO model and the user-defined WSGG model (combined with the band approach). The soot volume fraction $f_{v,soot}$ was varied between 10^{-7} and 10^{-3} while the soot constant C_{soot} was assumed to be 4.5, 5 or 5.5. The predicted radiation heat fluxes are shown in Fig. 15, and the radiation wall heat fluxes are compared in Table 12. First of all, the effect of the soot constant C_{soot} is negligible at soot volume fractions lower than 10^{-6}. However, with an increasing soot volume fraction $f_{v,soot}$ (up to 10^{-3}), the choice of the soot constant C_{soot} may alter the radiation wall heat flux predictions by as much as 20%. The effect of the soot volume fraction $f_{v,soot}$ on the radiation wall heat flux predictions is more pronounced. While an increase of the soot volume fraction $f_{v,soot}$ from zero to 10^{-6} decreases the radiation wall heat flux by around 25%, the decrease is stronger at a soot volume fraction $f_{v,soot}$ of 10^{-3} reaching around 35–50%.

The effects described above and presented in Fig. 15 and Table 12 require a careful interpretation. Firstly, as it has already been pointed out, no evidence of soot presence was observed in the bioliq EFG experiment considered in this study. Secondly, soot volume fractions above 10^{-5} correspond already to *sooty* conditions and are indications of imperfections in reactor/burner design. Thirdly, in the 1D slab-calculations, the soot volume fraction was prescribed by a value which did not vary along the path length which may be typical for far-flame regions only. In summary, the above presented considerations on soot are indicative and just flag up the issue. Judgement, whether soot is to be included or not, must be made on a case by case basis.

4.5. CFD simulations

CFD simulations were carried out (i) using the user-defined WSGG model for the bioliq EFG conditions and the band approach, (ii) using the user-defined WSGG model and the mean beam length approach and (iii) using the domain-based model. The results are compared in Fig. 16 using the total (radiation + convection) heat fluxes $\dot{q}_{tot}$ and

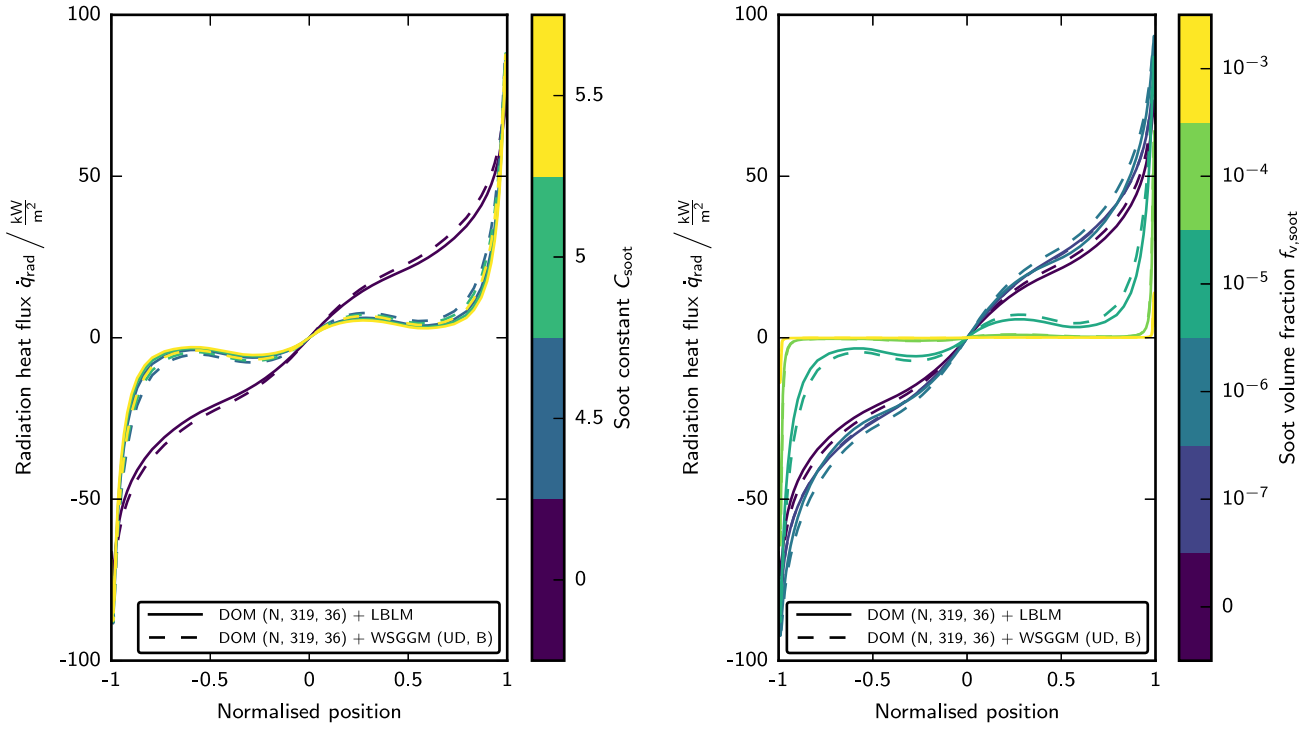

Fig. 15. Predicted radiation heat flux profiles for the bioliq EFG experiment V82.1 at the nozzle distance of 1524 mm based on 1D slab simulations for various soot constants C_{soot} at constant soot volume fraction $f_{v,soot} = 10^{-5}$ (left) and for various soot volume fractions $f_{v,soot}$ at constant soot constant $C_{soot} = 5$ (right).

Table 12
Predicted absolute radiation wall heat fluxes $|\dot{q}_{rad,wall}|$ for the bioliq EFG experiment V82.1 at the nozzle distance of 1524 mm based on 1D slab simulations with the DO model and the LBL model or the DO model and the user-defined WSGG model (combined with the band approach) and with various soot volume fractions $f_{v,soot}$ and with various soot constants C_{soot}.

$f_{v,soot}$	$\frac{\lvert\dot{q}_{rad,wall}\rvert}{kW/m^2}$					
	$C_{soot} = 4.5$		$C_{soot} = 5$		$C_{soot} = 5.5$	
	LBLM	WSGGM	LBLM	WSGGM	LBLM	WSGGM
0	66.50	69.97	66.50	69.97	66.50	69.97
10^{-7}	74.70	74.87	75.30	75.30	75.85	75.71
10^{-6}	84.22	86.18	84.07	86.35	83.88	86.43
10^{-5}	71.14	76.00	70.04	75.03	68.98	74.11
10^{-4}	32.46	38.04	30.34	35.63	28.46	33.46
10^{-3}	41.60	42.87	37.31	38.21	33.80	34.46

show a significant impact of the gas radiation property model on the predictions of the wall heat fluxes. This is in agreement with the results of the 1D slab simulations while the user-defined WSSG model combined with the band approach provides the best numerical results in comparison with the experimental results. Furthermore, the radiation wall heat fluxes $\dot{q}_{rad}$ at the nozzle distances of 260 mm and 1524 mm were extracted from the CFD simulations and are presented in Tables 13 and 14. In comparison with the radiation wall heat fluxes $\dot{q}_{rad,wall}$ predicted by the 1D slab simulations, similar predictions are made in values due to the optically thick conditions, in particular using the user-defined WSSG model combined with the band approach. 1D slab simulations are thus a good alternative for radiation wall heat flux estimations when average gas conditions are known.

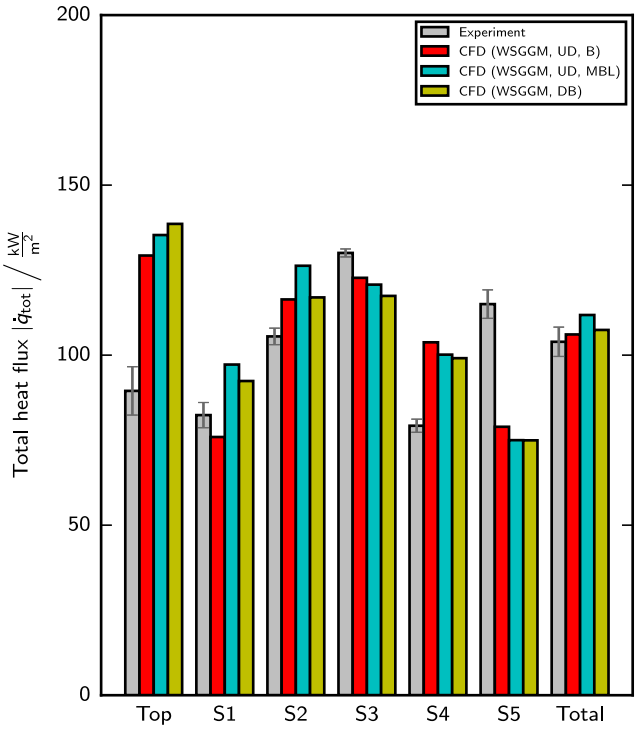

Fig. 16. Segmental and total heat fluxes for the bioliq EFG experiment V82.1 based on measurements and balances and on CFD simulations.

Table 13
Predicted absolute radiation wall heat fluxes $|\dot{q}_{rad,wall}|$ and predicted absolute total wall heat fluxes $|\dot{q}_{tot,wall}|$ for the bioliq EFG experiment V82.1 at the nozzle distance of 260 mm based on CFD simulations with the DO model and with various gas radiation property models.

Gas radiation property model	$\lvert\dot{q}_{rad,wall}\rvert$ / kW/m^2	$\lvert\dot{q}_{tot,wall}\rvert$ / kW/m^2
WSGGM (UD, B)	67.29	75.88
WSGGM (UD, MBL)	83.82	97.61
WSGGM (DB)	82.86	97.44

Table 14
Predicted absoulte radiation wall heat fluxes $|\dot{q}_{rad,wall}|$ and predicted absolute total wall heat fluxes $|\dot{q}_{tot,wall}|$ for the bioliq EFG experiment V82.1 at the nozzle distance 1524 mm based on CFD simulations with the DO model and with various gas radiation property models.

Gas radiation property model	$\lvert\dot{q}_{rad,wall}\rvert$ / kW/m^2	$\lvert\dot{q}_{tot,wall}\rvert$ / kW/m^2
WSGGM (UD, B)	75.67	114.94
WSGGM (UD, MBL)	74.04	111.29
WSGGM (DB)	68.58	109.09

5. Conclusions

Comparative one-dimensional slab and two-dimensional CFD simulations were performed in order to obtain an insight into thermal radiation at atmospheric and high-pressure entrained flow gasification conditions. The results show that simulations based on user-defined weighted-sum-of-grey-gas (WSGG) models combined with the band approach provide accurate predictions of the radiation heat flux and the radiation heat source term if the WSGG models are generated using appropriate line-by-line (LBL) calculations with the HITEMP-2010 databases [44].

Reasonable predictions of the radiation wall heat flux at high-pressure conditions were also provided by the WSGG model of Smith et al. [31] combined with the scaling rules of Edwards and Matavosian [32] and the mean beam length model [33]. However, this approach showed deficiencies in predicting the radiation heat flux and the radiation heat source term distributions at both atmospheric and high-pressure conditions. Customised WSGG models should thus be preferred over literature-based WSGG models if the latter have been developed for deviating conditions.

Further alternatives for customised WSGG models are spectral-line-weighted-sum-of-grey-gas (SLWSGG) models [34,35] and full-spectrum correlated-k distribution (FSCK) models [36]. In comparison with user-defined WSGG models combined with the band approach, SLWSGG and FSCK models are able to provide superior results at the expense of increased number of pseudo-bands and can be incorporated into CFD models without any elaborative ventures since the underlying tables and computing methods are available [85,86]. However, only the integration of FSCK models can be recommended for CFD simulations (alongside user-defined WSGG models combined with the band approach) since the calculation of absorption coefficients and weights using the available methods is significantly less expensive for FSCK than for SLWSGG models. As appropriate interfaces are not available for the most popular CFD software packages, future studies should establish, for example, user-defined functions for the application of FSCK models in ANSYS Fluent and absorptionEmission classes for the use of WSGG and FSCK models in OpenFOAM.

Accurate predictions of heat removal are essential for the design and scale-up of high-pressure entrained flow gasifiers. Therefore, the impact of radiation model simplifications and of uncertainties in the gas conditions were also investigated in this study. The analysis results demonstrated that a coarse discretisation of the radiative transfer equation in the boundary layer, the P-1 approximation and inaccurate gas species concentrations (within a $\pm 5\%$ margin) can be accepted while the contribution of soot has to be taken into account for soot volume fractions exceeding 10^{-6}. Soot concentrations should thus be determined experimentally, and judgement whether soot is to be included or not must be made on a case-by-case basis.

CRediT authorship contribution statement

Maximilian Dammann: Conceptualisation, Methodology, Software, Investigation, Validation, Formal analysis, Visualisation, Writing – original draft. **Marco Mancini:** Conceptualisation, Supervision. **Thomas Kolb:** Supervision, Project administration, Funding acquisition. **Roman Weber:** Writing – review & editing, Supervision, Project administration, Funding acquisition.

Declaration of competing interest

The authors declare that they have no known competing financial interests or personal relationships that could have appeared to influence the work reported in this paper.

Data availability

Data will be made available on request.

Acknowledgements

The authors thank (i) the Helmholtz Association of German Research Centres (HGF) for funding the programmes Energy Efficiency, Materials and Resources (EMR) and Materials and Technologies for the Energy Transition (MTET), (ii) Michael Alberti (formerly Clausthal University of Technology, Institute for Energy Process Engineering and Fuel Technology), John T. Pearson (formerly Brigham Young University, Department of Mechanical Engineering) and Chaoyun Wang (Beijing Jiaotong University, Institute of Combustion and Thermal Systems) for their preceding studies and (iii) David Böning, Sabine Fleck, Ulrike Santo and Hannah Schmid (Karlsruhe Institute of Technology, Institute for Technical Chemistry, Gasification Technology) and Mark Eberhard (formerly Karlsruhe Institute of Technology, Institute for Technical Chemistry, Gasification Technology) for the constant collaboration.

References

[1] N. Dahmen, J. Abeln, M. Eberhard, T. Kolb, H. Leibold, J. Sauer, D. Stapf, B. Zimmerlin, The bioliq process for producing synthetic transportation fuels, WIREs Energy Environ. 6 (3) (2016) http://dx.doi.org/10.1002/wene.236.

[2] M. Mancini, M. Alberti, M. Dammann, U. Santo, G. Eckel, T. Kolb, R. Weber, Entrained flow gasification. Part 2: Mathematical modeling of the gasifier using RANS method, Fuel 225 (2018) 596–611, http://dx.doi.org/10.1016/j.fuel.2018.03.100.

[3] M. Dammann, M. Mancini, S. Fleck, R. Weber, T. Kolb, Entrained flow gasification: Experiments and mathematical modelling based on RANS, in: Proceedings of the Joint Meeting the German and Italian Sections of the Combustion Institute, 24-26 May 2018, Sorrento, Italy, Italian Section of the Combustion Instititute, Sorrento, Italy, 2018, http://dx.doi.org/10.5445/IR/1000085909.

[4] M. Dammann, M. Mancini, S. Fleck, R. Weber, T. Kolb, Entrained flow gasification: Experiments and mathematical modelling based on RANS, in: Proceedings of the 29th Deutscher Flammentag: Verbrennung und Feuerung, 17-18 September 2019, Bochum, Germany, Deutsche Vereinigung für Verbrennungsforschung and The Combustion Institute Deutsche Sektion, Bochum, Germany, 2019, http://dx.doi.org/10.5445/IR/1000131589.

[5] U. Santo, D. Böning, M. Eberhard, H. Schmid, T. Kolb, Entrained flow gasification: experiments and balancing for design and scale-up, in: Proceedings of the 30th Deutscher Flammentag: Für nachhaltige Verbrennung, 28-29 September 2021, Hannover-Garbsen, Germany, Deutsche Vereinigung für Verbrennungsforschung and The Combustion Institute Deutsche Sektion, Hannover-Garbsen, Germany, 2021, http://dx.doi.org/10.5445/IR/1000139705.

[6] M. Dammann, M. Mancini, R. Weber, T. Kolb, Entrained flow gasification: mathematical modelling based on RANS for design and scale-up, in: Proceedings of the 30th Deutscher Flammentag: Für nachhaltige Verbrennung, 28-29 September 2021, Hannover-Garbsen, Germany, Deutsche Vereinigung für Verbrennungsforschung and The Combustion Institute Deutsche Sektion, Hannover-Garbsen, Germany, 2021, http://dx.doi.org/10.5445/IR/1000140359.

[7] M. Dammann, Numerical modelling and simulation of entrained flow gasification (Ph.D. thesis), Fakultät für Chemieingenieurwesen und Verfahrenstechnik, Karlsruher Institut für Technologie, Karlsruhe, Germany, 2023, (in preparation).

[8] X. Lu, T. Wang, Investigation of radiation models in entrained-flow coal gasification simulation, Int. J. Heat Mass Transfer 67 (2013) 377–392, http://dx.doi.org/10.1016/j.ijheatmasstransfer.2013.08.011.

[9] M. Marklund, Pressurized entrained-flow high temperature black liquor gasification: CFD based reactor scale-up method and spray burner characterization (Ph.D. thesis), Department of Engineering Sciences and Mathematics, Luleå University of Technology, Luleå, Sweden, 2006, URL https://nbn-resolving.org/urn:nbn:se:ltu:diva-26275.

[10] J. Ge, Z. Wang, K. Wan, Y. He, Z. Zhou, Z. Huang, Slagging behavior modeling in coal gasifiers using two-way coupled slag model with CFD, Fuel 281 (2020) 118736, http://dx.doi.org/10.1016/j.fuel.2020.118736.

[11] H.J. Jeong, D.K. Seo, J. Hwang, CFD modeling for coal size effect on coal gasification in a two-stage commercial entrained-bed gasifier with an improved char gasification model, Appl. Energy 123 (2014) 29–36, http://dx.doi.org/10.1016/j.apenergy.2014.02.026.

[12] H.J. Jeong, I.S. Hwang, S.S. Park, J. Hwang, Investigation on co-gasification of coal and biomass in Shell gasifier by using a validated gasification model, Fuel 196 (2017) 371–377, http://dx.doi.org/10.1016/j.fuel.2017.01.103.

[13] X. Lu, T. Wang, Simulation of ash deposition behavior in an entrained flow coal gasifier, Int. J. Clean Coal Energy 4 (2) (2015) 43–59, http://dx.doi.org/10.4236/ijcce.2015.42005.

[14] J. Ma, S.E. Zitney, Computational fluid dynamic modeling of entrained-flow gasifiers with improved physical and chemical submodels, Energy Fuels 26 (12) (2012) 7195–7219, http://dx.doi.org/10.1021/ef301346z.

[15] J. Mularski, N. Modliński, Impact of chemistry-turbulence interaction modeling approach on the CFD simulations of entrained flow coal gasification, Energies 13 (23) (2020) 6467, http://dx.doi.org/10.3390/en13236467.

[16] J. Mularski, N. Modliński, Entrained flow coal gasification process simulation with the emphasis on empirical devolatilization models optimization procedure, Appl. Therm. Eng. 175 (2020) 115401, http://dx.doi.org/10.1016/j.applthermaleng.2020.115401.

[17] J. Mularski, N. Modliński, Entrained-flow coal gasification process simulation with the emphasis on empirical char conversion models optimization procedure, Energies 14 (6) (2021) 1729, http://dx.doi.org/10.3390/en14061729.

[18] P. Nakod, CFD modeling and validation of oxy-fired and air-fired entrained flow gasifiers, Int. J. Chem. Phys. Sci. 2 (6) (2013) 28–40, URL https://www.ijcps.org/0Site/issue8.html.

[19] S. Park, H. Jeong, J. Hwang, 3-D CFD modeling for parametric study in a 300-MW one-stage oxygen-blown entrained-bed coal gasifier, Energies 8 (5) (2015) 4216–4236, http://dx.doi.org/10.3390/en8054216.

[20] A. Rashidi, CFD Simulation of Biomass Gasification Using Detailed Chemistry (Ph.D. thesis), Ruprecht-Karls-Universität Heidelberg, Naturwissenschaftlich-Mathematische Gesamtfakultät der Ruprecht-Karls-Universität Heidelberg, Heidelberg, Germany, 2011, http://dx.doi.org/10.11588/heidok.00011654.

[21] M. Saiful Alam, A.T. Wijayanta, K. Nakaso, J. Fukai, Study on coal gasification with soot formation in two-stage entrained-flow gasifier, Int. J. Energy Environ. Eng. 6 (3) (2015) 255–265, http://dx.doi.org/10.1007/s40095-015-0173-1.

[22] S. Schulze, A. Richter, M. Vascellari, A. Gupta, B. Meyer, P.A. Nikrityuk, Novel intrinsic-based submodel for char particle gasification in entrained-flow gasifiers: Model development, validation and illustration, Appl. Energy 164 (2016) 805–814, http://dx.doi.org/10.1016/j.apenergy.2015.12.018.

[23] Z. Sun, Z. Dai, Z. Zhou, Q. Guo, G. Yu, Numerical simulation of industrial opposed multiburner coal-water slurry entrained flow gasifier, Ind. Eng. Chem. Res. 51 (6) (2012) 2560–2569, http://dx.doi.org/10.1021/ie201542q.

[24] H. Tominaga, T. Yamashita, T. Ando, N. Asahiro, Simulator development of entrained flow coal gasifiers at high temperature and high pressure atmosphere, IFRF Combust. J. (200004) (2000) URL http://citeseerx.ist.psu.edu/doc_view/pid/64885ec38b851e7c80371b1e7d5ca28f768ed63e.

[25] M. Vascellari, R. Arora, M. Pollack, C. Hasse, Simulation of entrained flow gasification with advanced coal conversion submodels. Part 1: Pyrolysis, Fuel 113 (2013) 654–669, http://dx.doi.org/10.1016/j.fuel.2013.06.014.

[26] M. Vascellari, R. Arora, C. Hasse, Simulation of entrained flow gasification with advanced coal conversion submodels. Part 2: Char conversion, Fuel 118 (2014) 369–384, http://dx.doi.org/10.1016/j.fuel.2013.11.004.

[27] M. Vascellari, D.G. Roberts, S.S. Hla, D.J. Harris, C. Hasse, From laboratory-scale experiments to industrial-scale CFD simulations of entrained flow coal gasification, Fuel 152 (2015) 58–73, http://dx.doi.org/10.1016/j.fuel.2015.01.038.

[28] L. Wang, Y. Jia, S. Kumar, R. Li, R.B. Mahar, M. Ali, I.N. Unar, U. Sultan, K. Memon, Numerical analysis on the influential factors of coal gasification performance in two-stage entrained flow gasifier, Appl. Therm. Eng. 112 (2017) 1601–1611, http://dx.doi.org/10.1016/j.applthermaleng.2016.10.122.

[29] ANSYS, ANSYS Fluent Theory Guide. Release 2020 R2, SAS IP, Canonsburg, PA, USA, 2020.

[30] ANSYS, ANSYS fluent. Release 2020 R2, 2020, URL http://www.ansys.com/products/fluids/ansys-fluent.

[31] T.F. Smith, Z.F. Shen, J.N. Friedman, Evaluation of coefficients for the weighted sum of gray gases model, J. Heat Transfer 104 (4) (1982) 602–608, http://dx.doi.org/10.1115/1.3245174.

[32] D.K. Edwards, R. Matavosian, Scaling rules for total absorptivity and emissivity of gases, J. Heat Transfer 106 (4) (1984) 684–689, http://dx.doi.org/10.1115/1.3246739.

[33] H.C. Hottel, A.F. Sarofim, Radiative Transfer, 1967.

[34] J.T. Pearson, The development of updated and improved SLW model parameters and its application to comprehensive combustion predictions (Ph.D. thesis), Department of Mechanical Engineering, Brigham Young University, Provo, UT, USA, 2013, URL http://hdl.lib.byu.edu/1877/etd6527.

[35] J.T. Pearson, B.W. Webb, V.P. Solovjov, J. Ma, Efficient representation of the absorption line blackbody distribution function for H_2O, CO_2, and CO at variable temperature, mole fraction, and total pressure, J. Quant. Spectrosc. Radiat. Transfer 138 (2014) 82–96, http://dx.doi.org/10.1016/j.jqsrt.2014.01.019.

[36] C. Wang, B. He, M.F. Modest, T. Ren, Efficient full-spectrum correlated-k-distribution look-up table, J. Quant. Spectrosc. Radiat. Transfer 219 (2018) 108–116, http://dx.doi.org/10.1016/j.jqsrt.2018.04.002.

[37] C. Wang, M.F. Modest, B. He, Full-spectrum correlated-k-distribution look-up table for use with radiative Monte Carlo solvers, Int. J. Heat Mass Transfer 131 (2019) 167–175, http://dx.doi.org/10.1016/j.ijheatmasstransfer.2018.10.133.

[38] C. Wang, B. He, M.F. Modest, Full-spectrum correlated-k-distribution look-up table for radiative transfer in nonhomogeneous participating media with gas-particle mixtures, Int. J. Heat Mass Transfer 137 (2019) 1053–1063, http://dx.doi.org/10.1016/j.ijheatmasstransfer.2019.03.149.

[39] F.R. Coelho, F.H.R. França, WSGG correlations based on HITEMP2010 for gas mixtures of H_2O and CO_2 in high total pressure conditions, Int. J. Heat Mass Transfer 127 (2018) 105–114, http://dx.doi.org/10.1016/j.ijheatmasstransfer.2018.07.075.

[40] S. Shan, B. Qian, Z. Zhou, Z. Wang, K. Cen, New pressurized WSGG model and the effect of pressure on the radiation heat transfer of H_2O/CO_2 gas mixtures, Int. J. Heat Mass Transfer 121 (2018) 999–1010, http://dx.doi.org/10.1016/j.ijheatmasstransfer.2018.01.079.

[41] B. Wang, Y. Xuan, An improved WSGG model for exhaust gases of aero engines within broader ranges of temperature and pressure variations, Int. J. Heat Mass Transfer 136 (2019) 1299–1310, http://dx.doi.org/10.1016/j.ijheatmasstransfer.2019.03.105.

[42] H. Bordbar, F.R. Coelho, G.C. Fraga, F.H.R. França, S. Hostikka, Pressure-dependent weighted-sum-of-gray-gases models for heterogeneous CO_2-H_2O mixtures at sub- and super-atmospheric pressure, Int. J. Heat Mass Transfer 173 (2021) 121207, http://dx.doi.org/10.1016/j.ijheatmasstransfer.2021.121207.

[43] Z. Yang, A. Gopan, Improved global model for predicting gas radiative properties over a wide range of conditions, Therm. Sci. Eng. Prog. 22 (2021) 100856, http://dx.doi.org/10.1016/j.tsep.2021.100856.

[44] L.S. Rothman, I.E. Gordon, R.J. Barber, H. Dothe, R.R. Gamache, A. Goldman, V.I. Perevalov, S.A. Tashkun, J. Tennyson, HITEMP, the high-temperature molecular spectroscopic database, J. Quant. Spectrosc. Radiat. Transfer 111 (15) (2010) 2139–2150, http://dx.doi.org/10.1016/j.jqsrt.2010.05.001.

[45] M.Y. Perrin, J.M. Hartmann, Temperature-dependent measurements and modeling of absorption by CO_2-N_2 mixtures in the far line-wings of the 4.3 μ m CO_2 band, J. Quant. Spectrosc. Radiat. Transfer 42 (4) (1989) 311–317, http://dx.doi.org/10.1016/0022-4073(89)90077-0.

[46] J.M. Hartmann, M.Y. Perrin, Q. Ma, R.H. Tippings, The infrared continuum of pure water vapor: Calculations and high-temperature measurements, J. Quant. Spectrosc. Radiat. Transfer 49 (6) (1993) 675–691, http://dx.doi.org/10.1016/0022-4073(93)90010-f.

[47] C. Brodbeck, J.P. Bouanich, N. Van-Thanh, J.M. Hartmann, B. Khalil, R.L. Doucen, Absorption of radiation by gases from low to high pressures. II. Measurements and calculations of CO infrared spectra, J. Phys. II 4 (12) (1994) 2101–2118, http://dx.doi.org/10.1051/jp2:1994249.

[48] F.R. Westlye, B.A.K. Hartz, A. Ivarsson, A. Fateev, S. Clausen, Evaluation of spectral radiative properties of gases in high-pressure combustion, J. Quant. Spectrosc. Radiat. Transfer 280 (2022) 108089, http://dx.doi.org/10.1016/j.jqsrt.2022.108089.

[49] M. Alberti, R. Weber, M. Mancini, Re-creating Hottel's emissivity charts for carbon dioxide and extending them to 40 bar pressure using HITEMP-2010 data base, Combust. Flame 162 (3) (2015) 597–612, http://dx.doi.org/10.1016/j.combustflame.2014.09.005.

[50] M. Alberti, R. Weber, M. Mancini, Re-creating Hottel's emissivity charts for water vapor and extending them to 40 bar pressure using HITEMP-2010 data base, Combust. Flame 169 (2016) 141–153, http://dx.doi.org/10.1016/j.combustflame.2016.04.013.

[51] M. Alberti, R. Weber, M. Mancini, Absorption of infrared radiation by carbon monoxide at elevated temperatures and pressures. Part A: Advancing the line-by-line procedure based on HITEMP-2010, J. Quant. Spectrosc. Radiat. Transfer 200 (2017) 258–271, http://dx.doi.org/10.1016/j.jqsrt.2017.05.024.

[52] M. Alberti, R. Weber, M. Mancini, Absorption of infrared radiation by carbon monoxide at elevated temperatures and pressures. Part B: Total emissivity charts and correlations, J. Quant. Spectrosc. Radiat. Transfer 200 (2017) 272–279, http://dx.doi.org/10.1016/j.jqsrt.2017.05.034.

[53] M. Alberti, R. Weber, M. Mancini, Gray gas emissivities for H_2O-CO_2-CO-N_2 mixtures, J. Quant. Spectrosc. Radiat. Transfer 219 (2018) 274–291, http://dx.doi.org/10.1016/j.jqsrt.2018.08.008.

[54] M. Alberti, Total Emissivity Charts for H_2O, CO_2 and CO from low to high pressures (Ph.D. thesis), Papierflieger, Fakultät für Energie- und Wirtschaftswissenschaften, Technische Universität Clausthal, Clausthal-Zellerfeld, Germany, 2018.

[55] S. Fleck, U. Santo, C. Hotz, T. Jakobs, G. Eckel, M. Mancini, R. Weber, T. Kolb, Entrained flow gasification. Part 1: Gasification of glycol in an atmospheric-pressure experimental rig, Fuel 217 (2018) 306–319, http://dx.doi.org/10.1016/j.fuel.2017.12.077.

[56] M. Eberhard, U. Santo, B. Michelfelder, A. Günther, P. Weigand, J. Matthes, P. Waibel, V. Hagenmeyer, T. Kolb, The bioliq® Entrained Flow Gasifier: A model for the German Energiewende, ChemBioEng Rev. 7 (4) (2020) 106–118, http://dx.doi.org/10.1002/cben.202000006.

[57] R. Demarco, J.L. Consalvi, A. Fuentes, S. Melis, Assessment of radiative property models in non-gray sooting media, Int. J. Therm. Sci. 50 (9) (2011) 1672–1684, http://dx.doi.org/10.1016/j.ijthermalsci.2011.03.026.

[58] M.F. Modest, Radiative Heat Transfer, third ed., Academic Press, 2013.

[59] J.L. Consalvi, F. Andre, F.R. Coelho, F.H.R. Franca, F. Nmira, M. Galtier, V. Solovjov, B.W. Webb, Assessment of engineering gas radiative property models in high pressure turbulent jet diffusion flames, J. Quant. Spectrosc. Radiat. Transfer 253 (2020) 107169, http://dx.doi.org/10.1016/j.jqsrt.2020.107169.

[60] P.J. Coelho, Advances in the discrete ordinates and finite volume methods for the solution of radiative heat transfer problems in participating media, J. Quant. Spectrosc. Radiat. Transfer 145 (2014) 121–146, http://dx.doi.org/10.1016/j.jqsrt.2014.04.021.

[61] W.H. Press, S.A. Teukolsky, W.T. Vetterling, B.P. Flannery, Numerical recipes in C: The art of scientific computing, second ed., Cambridge University Press, Cambridge, UK, 2002.

[62] B.E. Launder, D.B. Spalding, Lectures in mathematical models of turbulence, Academic Press, London, UK [et al.], 1972.

[63] B.E. Launder, D.B. Spalding, The numerical computation of turbulent flows, Comput. Methods Appl. Mech. Engrg. 3 (2) (1974) 269–289, http://dx.doi.org/10.1016/0045-7825(74)90029-2.

[64] S.V. Patankar, D.B. Spalding, A calculation procedure for heat, mass and momentum transfer in three-dimensional parabolic flows, Int. J. Heat Mass Transfer 15 (10) (1972) 1787–1806, http://dx.doi.org/10.1016/0017-9310(72)90054-3.

[65] B. Magnussen, On the structure of turbulence and a generalized eddy dissipation concept for chemical reaction in turbulent flow, in: Proceedings of the 19th Aerospace Sciences Meeting, 12-15 January 1981, St. Louis, MO, USA, (81–31510) American Institute of Aeronautics and Astronautics, St. Louis, MO, USA, 1981, http://dx.doi.org/10.2514/6.1981-42.

[66] E.H. Chui, G.D. Raithby, Computation of radiant heat transfer on a nonorthogonal mesh using the finite-volume method, Numer. Heat Transfer B 23 (3) (1993) 269–288, http://dx.doi.org/10.1080/10407799308914901.

[67] J.Y. Murthy, S.R. Mathur, Finite volume method for radiative heat transfer using unstructured meshes, J. Thermophys. Heat Transfer 12 (3) (1998) 313–321, http://dx.doi.org/10.2514/2.6363.

[68] M. Seggiani, Modelling and simulation of time varying slag flow in a Prenflo entrained-flow gasifier, Fuel 77 (14) (1998) 1611–1621, http://dx.doi.org/10.1016/s0016-2361(98)00075-1.

[69] D.K. Edwards, Molecular gas band radiation, in: Advances in Heat Transfer, Elsevier, 1976, pp. 115–193, http://dx.doi.org/10.1016/s0065-2717(08)70163-1.

[70] A.T. Modak, Exponential wide band parameters for the pure rotational band of water vapor, J. Quant. Spectrosc. Radiat. Transfer 21 (2) (1979) 131–142, http://dx.doi.org/10.1016/0022-4073(79)90024-4.

[71] MathWorks, MATLAB. Release R2019b, 2018.

[72] T. Jakobs, N. Djordjevic, S. Fleck, M. Mancini, R. Weber, T. Kolb, Gasification of high viscous slurry. R&D on atomization and numerical simulation, Appl. Energy 93 (2012) 449–456, http://dx.doi.org/10.1016/j.apenergy.2011.12.026.

[73] M. Mancini, R. Weber, P. Weigand, W. Leuckel, T. Kolb, Design of the entrained flow reactor for gasification of biomass based slurry, in: Proceedings of the 26th Deutscher Flammentag: Verbrennung und Feuerung, 11-12 September 2013, Duisburg, Germany, in: VDI-Berichte, vol. 2161, VDI-Verlag, Düsseldorf, Germany, 2013, pp. 625–634.

[74] N. Lallemant, R. Weber, A computationally efficient procedure for calculating gas radiative properties using the exponential wide band model, Int. J. Heat Mass Transfer 39 (15) (1996) 3273–3286, http://dx.doi.org/10.1016/0017-9310(95)00400-9.

[75] C. Wang, M.F. Modest, B. He, Improvement of full-spectrum k-distribution method using quadrature transformation, Int. J. Therm. Sci. 108 (2016) 100–107, http://dx.doi.org/10.1016/j.ijthermalsci.2016.05.005.

[76] J.D. Felske, C.L. Tien, The use of the Milne-Eddington absorption coefficient for radiative heat transfer in combustion systems, J. Heat Transfer 99 (3) (1977) 458–465, http://dx.doi.org/10.1115/1.3450718.

[77] S. Fleck, K.P. Geigle, C. Hotz, K. Peter, T. Kolb, Formation and decay of hydrocarbon intermediates in an entrained flow gasifier, in: Proceedings of the 27th Deutscher Flammentag: Verbrennung und Feuerung, 16-17 September 2015, Clausthal-Zellerfeld, Germany, in: VDI-Berichte, vol. 2267, VDI-Verlag, Düsseldorf, Germany, 2015, pp. 207–218.

[78] A. Sepman, Y. Ögren, M. Gullberg, H. Wiinikka, Development of TDLAS sensor for diagnostics of CO, H_2O and soot concentrations in reactor core of pilot-scale gasifier, Appl. Phys. B 122 (29) (2016) http://dx.doi.org/10.1007/s00340-016-6319-x.

[79] J. Simonsson, H. Bladh, M. Gullberg, E. Pettersson, A. Sepman, Y. Ögren, H. Wiinikka, P.-E. Bengtsson, Soot concentrations in an atmospheric entrained flow gasifier with variations in fuel and burner configuration studied using diode-laser extinction measurements, Energy Fuels 30 (3) (2016) 2174–2186, http://dx.doi.org/10.1021/acs.energyfuels.5b02561.

[80] B. Göktepe, K. Umeki, A. Hazim, T.S. Lundström, R. Gebart, Soot reduction in an entrained flow gasifier of biomass by active dispersion of fuel particles, Fuel 201 (2017) 111–117, http://dx.doi.org/10.1016/j.fuel.2016.09.039.

[81] A. Bader, M. Hartwich, A. Richter, B. Meyer, Numerical and experimental study of heavy oil gasification in an entrained-flow reactor and the impact of the burner concept, Fuel Process. Technol. 169 (2018) 58–70, http://dx.doi.org/10.1016/j.fuproc.2017.09.003.

[82] P. Virtanen, R. Gommers, T.E. Oliphant, M. Haberland, T. Reddy, D. Cournapeau, E. Burovski, P. Peterson, W. Weckesser, J. Bright, S.J. van der Walt, M. Brett, J. Wilson, K.J. Millman, N. Mayorov, A.R.J. Nelson, E. Jones, R. Kern, E. Larson, C.J. Carey, İ. Polat, Y. Feng, E.W. Moore, J. VanderPlas, D. Laxalde, J. Perktold, R. Cimrman, I. Henriksen, E.A. Quintero, C.R. Harris, A.M. Archibald, A.H. Ribeiro, F. Pedregosa, P. van Mulbregt, S.. Contributors, SciPy 1.0: Fundamental algorithms for scientific computing in Python, Nature Methods 17 (2020) 261–272, http://dx.doi.org/10.1038/s41592-019-0686-2.

[83] SciPy Developers, SciPy. Release 1.5.1, Python Software Foundation, 2021, URL https://pypi.org/project/scipy/.

[84] J. Mularski, H. Pawlak-Kruczek, N. Modlinski, A review of recent studies of the CFD modelling of coal gasification in entrained flow gasifiers, covering devolatilization, gas-phase reactions, surface reactions, models and kinetics, Fuel 271 (2020) 117620, http://dx.doi.org/10.1016/j.fuel.2020.117620.

[85] J.T. Pearson, Absorption line blackbody distribution function, 2013, URL https://albdf.byu.edu/.

[86] P.R. Somesh, Data and software related to radiative transfer, 2023, URL https://www.eng.mu.edu/ccl/software-data/radiation/.